DOE SBIR/STTR Phase I Final Report

Topic 2: Increasing Adoption of HPC Modeling and Simulation in the Advanced Manufacturing and Engineering Industries
Subtopic a: Turnkey HPC Solutions for Manufacturing and Engineering

Project Title
Optimization Using Metamodeling in the Context of Integrated Computational Materials Engineering (ICME)

Phase I Grant Award Number
DE-SC0009687

Principal Investigator
Dr. Youssef Hammi

Company Name & Address
Predictive Design Technologies, LLC
60 Technology Boulevard, Suite 115B
Starkville, MS 39759

Collaborator
Center for Advanced Vehicular Systems
Mississippi State University

Industrial Partner
Plymouth Tube Company

Table of Contents

1 EXECUTIVE SUMMARY

Predictive Design Technologies, LLC (PDT) proposed to employ Integrated Computational Materials Engineering (ICME) tools to help the manufacturing industry in the United States regain the competitive advantage in the global economy. ICME uses computational materials science tools within a holistic system in order to accelerate materials development, improve design optimization, and unify design and manufacturing. With the advent of accurate modeling and simulation along with significant increases in high performance computing (HPC) power, virtual design and manufacturing using ICME tools provide the means to reduce product development time and cost by alleviating costly trial-and-error physical design iterations while improving overall quality and manufacturing efficiency. To reduce the computational cost necessary for the large-scale HPC simulations and to make the methodology accessible for small and medium-sized manufacturers (SMMs), metamodels are employed. Metamodels are approximate models (functional relationships between input and output variables) that can reduce the simulation times by one to two orders of magnitude.

In Phase I, PDT, partnered with Mississippi State University (MSU), demonstrated the feasibility of the proposed methodology by employing MSU's internal state variable (ISV) plasticity-damage model with the help of metamodels to optimize the microstructure-process-property-cost for tube manufacturing processes used by Plymouth Tube Company (PTC), which involves complicated temperature and mechanical loading histories.

PDT quantified the microstructure-property relationships for PTC's SAE J525 electric resistance-welded cold drawn low carbon hydraulic 1010 steel tube manufacturing processes at seven different material states and calibrated the ISV plasticity material parameters to fit experimental tensile stress-strain curves. PDT successfully performed large scale finite element (FE) simulations in an HPC environment using the ISV plasticity model in Abaqus FE analyses of the tube forming, sizing, drawing, welding, and normalizing processes. The simulation results coupled with the manufacturing cost data were used to develop prototype metamodeling (quick response) codes which could be used to predict and optimize the microstructure-process-property-cost relationships. The developed ICME metamodeling toolkits are flexible enough to be applied to other manufacturing processes (e.g. forging, forming, casting, extrusion, rolling, stamping, and welding/joining) and metamodeling codes can run on laptop computers.

Based on the work completed in Phase I, in Phase II, PDT proposes to continue to refine the ISV model by correlating and incorporating the uncertainties in the microstructure, mechanical testing, and modeling. Following the model refinement, FE analyses will be simulated and will provide even more realistic predictions as they include an appropriate window of uncertainty. Using the HPC output (FE analyses) as input, the quick-response metamodel codes will more accurately predict and optimize the microstructure-process-property-cost relationships. Furthermore, PDT propose to employ the ICME metamodeling toolkits to help develop a new tube product using entirely new high strength steel. The modeling of the high strength steel manufacturing process will replace the costly and time consuming trial-and-error methods that were used in the tubing industry previously. This simulation-based process prototyping will greatly benefit our industrial partners by opening up new market spaces due to new products with greater capabilities.

2 PHASE I OBJECTIVES

Predictive Design Technologies, LLC (PDT) proposed to employ Integrated Computational Materials Engineering (ICME) tools to enable rapid improvement in the United States' manufacturing industry. The ultimate goal of the proposed research is to develop metamodeling (quick response) codes that can be used on laptop computers. These metamodeling codes are calibrated with the results from large-scale finite element simulations which require high performance computing (HPC) environments to run an internal state variable plasticity-damage model that can captures history effects in material processing and performance.

In Phase I, PDT, partnered with Mississippi State University (MSU), employed MSU's internal state variable (ISV) multiscale modeling with the help of metamodels to optimize the microstructure-process-property-cost for a tube drawing process. The drawing process was defined by Plymouth Tube Company (PTC), which involves complicated temperature and mechanical loading histories.

The specific objectives and tasks for Phase I are listed as follows:

Objective/Task 1: ISV Plasticity-Damage Model Calibration and Validation

- Task 1.1 Quantify the microstructure-property relationships throughout the Plymouth Tubing process for 1010 steel
- Task 1.2 Correlate the ISV model constants to the 1010 steel with tension, torsion and compression experimental data including uncertainty errors
- Task 1.3 Validate the ISV model constants with notch tensile tests of 1010 steel including uncertainty errors

Objective/Task 2: Large Scale Finite Element Simulations in HPC Environment

- Task 2.1 Simulations using ISV theory in ABAQUS of forming process
- Task 2.2 Simulations using ISV theory in ABAQUS of welding process initialized by forming results
- Task 2.3 Simulations using ISV theory in ABAQUS of normalization process initialized by welding results
- Task 2.4 Simulations using ISV theory in ABAQUS of the drawing process initialized by normalization results

Objective/Task 3: Metamodel Development

- Task 3.1 Evaluate several metamodels for best fits to finite element and HSMM simulations throughout tube processing history
- Task 3.2 Include uncertainty parameters into metamodel
- Task 3.3 Include cost model into metamodel

The accomplishments of these objectives and tasks for Phase I are described in following sections.

3 PHASE I ACCOMPLISHMENTS

In Phase I, PDT accomplished the following:

- Quantified microstructure-property relationships for PTC's SAE J525 electric resistance-welded cold drawn low carbon hydraulic 1010 steel tube manufacturing processes at seven different material states.
- Calibrated ISV plasticity material parameters to fit experimental tensile stress-strain curves.
- Performed large scale finite element (FE) simulations in an HPC environment using an ISV plasticity model in Abaqus of the tube forming, sizing, and drawing processes.
- Developed metamodels from tube forming process data using SUMO.
- Developed prototype software implementing 'microstructure-process-property-cost' relationships, using MATLAB-Simulink and the forming process metamodel.

These results prove the feasibility of the proposed methodology. The work accomplished in Phase I built a sound foundation for the development of a complete ICME metamodeling toolkit for Phase II of the project.

The details of the work done in Phase I with respect to each task are described in the following sections.

4 METHODS, ASSUMPTIONS, AND PORCEDURES

4.1 PTC'S TUBE MANUFACTURING PROCESSES

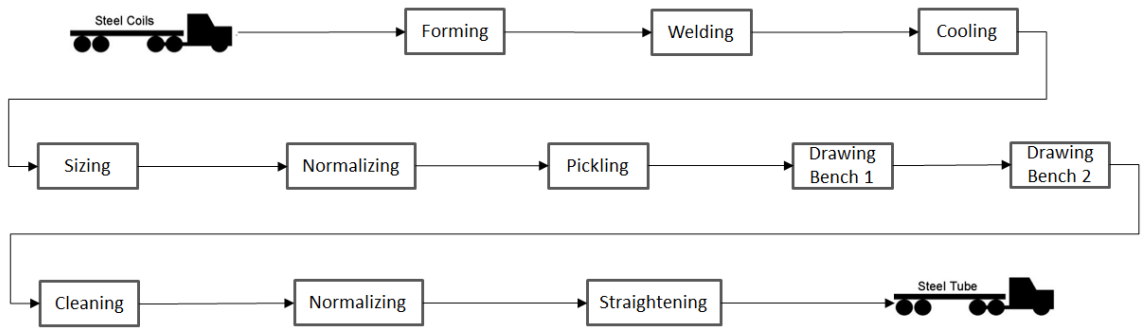

Figure 1. Plymouth Tube Company's (PTC) current manufacturing process.

PTC's manufacturing process of SAE J525 electric resistance-welded cold drawn low carbon hydraulic 1010 steel tube can be broken down into eleven steps (as illustrated in Figure 1). It begins with coils of 1010 steel sheet in the weld mill, which are cut to the proper width for the desired tube size. The cut strip, or skelp, passes through a series of rolls that progressively cold-form it into a tubular shape. It then passes through an electric resistance welder to join the seam together, under pressure, to complete the tubular shape. The tubes then enter the sizing section of the weld mill where a series of rollers fine tune the outside diameter of the newly formed tubes. Eddy current is used to detect any imperfections in the

tubes as they exit the weld mill with a 1.000" outer diameter and 0.105" wall thickness. Once the tubes leave the weld mill, they are placed in a roller-hearth furnace for a heat treatment process.

The tubes are heated past the austenizing region to a temperature of 1700°F/927°C to ensure grain recrystallization. They are then allowed to slowly cool to room temperature in an atmosphere of 10% hydrogen and 90% nitrogen. The tubes then go through a pickling line in which a series of six tanks apply a lubricant to the surface of the tube. After the lubricant has been applied to the tubes, they are brought to the draw bench. At the draw bench, hydraulic pressure is used to crimp the end of the tubes creating a smaller diameter on the tube ends. This smaller diameter is needed so that the tubes can be fed through the outside diameter (OD) drawing die. Once pointed, the tube is pulled through a die and over a mandrel at room temperature. This reduces the high volume part to an intermediate dimension with an OD of 0.813" and an inside diameter (ID) of 0.650" – 0.653". The tubes are then drawn a second time through another die but with no mandrel controlling the inner diameter. When the tubes exit the draw bench, they have an OD of 0.502" and a 0.081" – 0.085" wall thickness.

The tubes are then sent to a cleaner line where the residual lubricant is removed. Once the tubes are cleaned they then go through the final annealing process. This is the same as the earlier heat treatment process. The tubes are heated to a temperature of 1700°F/927°C and allowed to slowly cool to room temperature in an atmosphere of 10% hydrogen and 90% nitrogen.

The final step is for the tubes to undergo a straightening process. The straightener uses a series of offset rolls to straighten the tube. The pressure causes the OD to decrease by 0.0005" to 0.001". Eddy Current is used to detect any imperfections and the tubes are cut to a final length specified by the customer. A rust preventative oil is applied, and then they are packed for final transport.

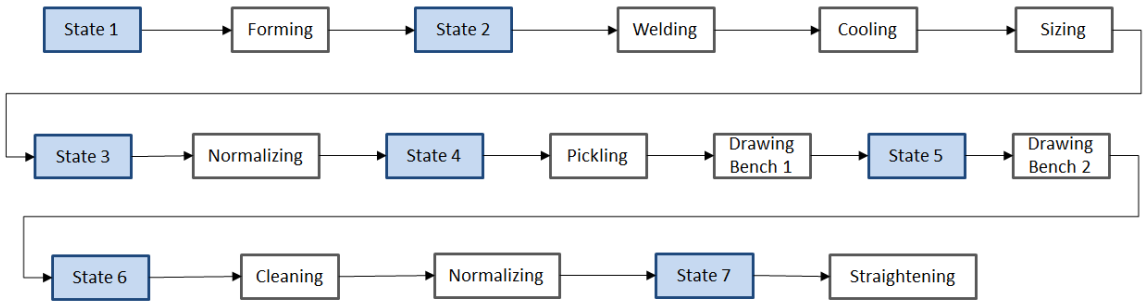

Figure 2. The seven material states used to quantify the microstructure-property relationships of PTC's manufacturing process.

The eleven steps shown in Figure 1 leave twelve material states to evaluate. Since the pickling, cleaning, and straightening steps listed above do not consist of a significant load or temperature change, the microstructure and mechanical property change during these steps were considered negligible. Thus the number of steps being evaluated could be reduced to eight. Also, since the welding, cooling, and sizing steps all occur within the weld

mill, they were considered one continuous step and the evaluation could then be simplified to just six manufacturing steps, and therefore seven material states, as seen in Figure 2.

4.2 MICROSTRUCTURE CHARACTERIZATION

PTC supplied tube samples from each of the material states listed in Figure 2 to be used in the microstructure analysis. Each of the tube samples were from the same batch of tubes throughout the manufacturing process. This ensures that a complete material history was considered in the analysis. The tube samples were then cut into three different sample orientations that were used to evaluate the microstructure. Figure 3 shows the sample orientations of the State 1 (Steel Coil) material, Figure 4 shows the sample orientations of the State 2 (After Forming) material, and Figure 5 shows the sample orientations of the remainder of the material states from after the tubes have been welded.

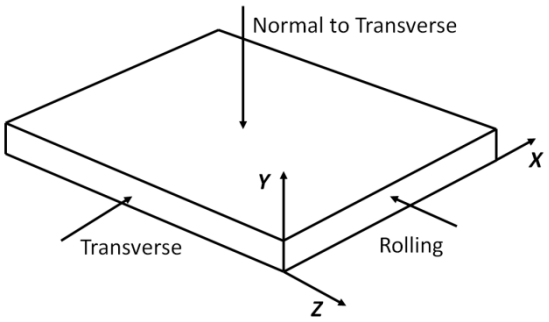

Figure 3. State 1 (Steel Coil) sample orientation schematic.

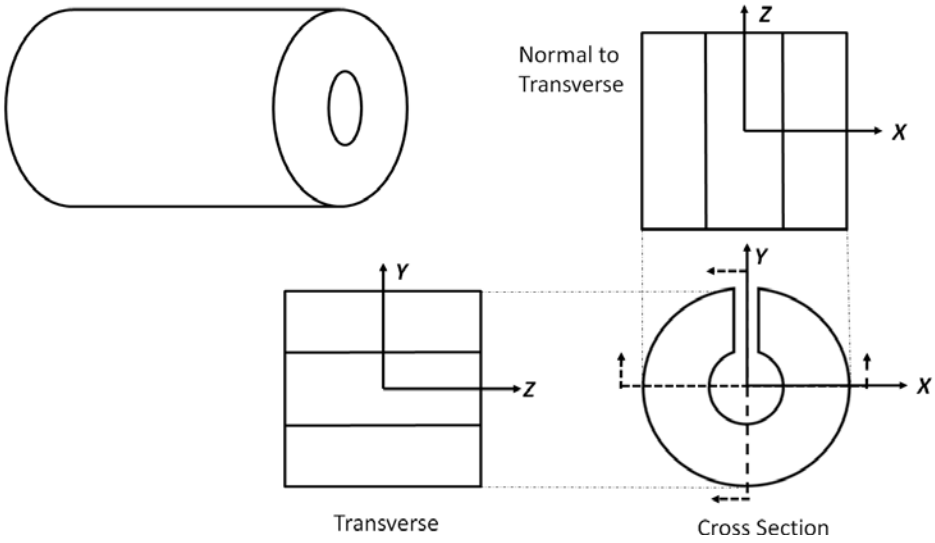

Figure 4. State 2 (After Forming) sample orientation schematic.

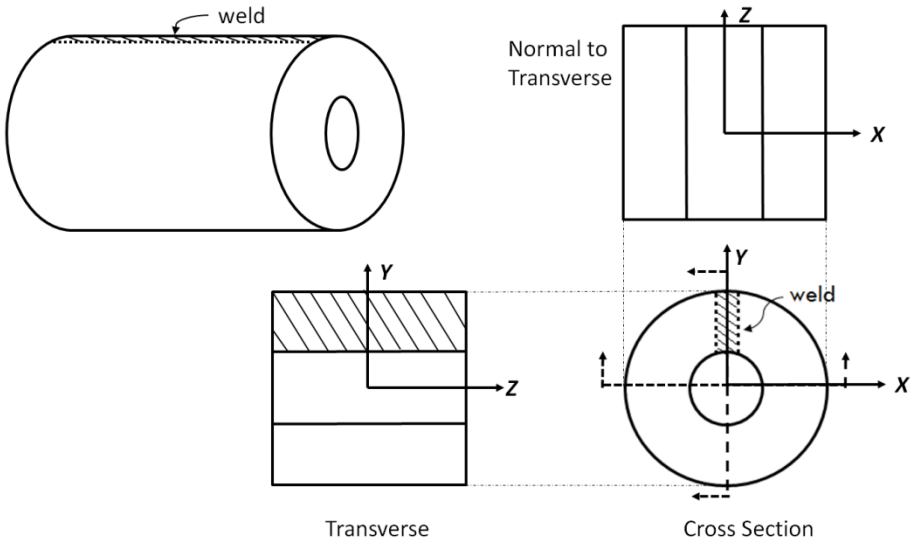

Figure 5. States 3–7 sample orientation schematic.

Once the tubes were cut into the three different sample orientations at each material state, they were then cold mounted using EpoFix hardener and resin inside of a vacuum. The mounted samples were then ground down to a flat surface to prepare for polishing. Once a pristine surface was present on all of the material samples, they were etched using standard etching techniques to expose the microstructure of the steel. The etchant applied was a 2% Nital solution for five seconds per sample (duration varies depending on the results). The samples were then cleaned and were ready for examination.

A Zeiss Axiovert 200M optical microscope was used to examine the microstructure. Several images were stitched together to create overview images of the samples in each orientation at each material state. Then detailed images were taken at different points on the samples to get a better understanding how each process parameter affects the microstructure of the steel.

4.3 MECHANICAL TESTS

Typical dog bone shaped tensile specimens were cut from the State 1 (Steel Coil) material and the rest of the six tube states in the rolling direction. An Instron EM Model 5882 dual column, load frame was used to perform tensile tests at room temperature. The tests were run at a strain rate of 0.001 per second with the cross-head being the controlling mechanism. Three test specimens were tested for each of the seven material states. This produced three stress-strain curves for each state. Matlab was used to obtain average stress-strain data from these curves. Uncertainty bands were placed at the yield strength, the ultimate tensile strength, and the elongation at failure for each of the average stress-strain curves.

4.4 INTERNAL STATE VARIABLE PLASTICITY MATERIAL MODEL

In order to model the sequential processing steps of materials, the history dependence of the stresses, strains, and microstructural content must be included to capture high fidelity solutions [Horstemeyer and Wang, 2003]. Key to the modeling and simulation of the sequential processes is the constitutive model. One modeling framework that can indeed capture the history dependence is that of the internal state variable (ISV) plasticity-damage theory based upon multiscale materials modeling. Although there are several ISV theories, one of the most successful was that developed at the Department of Energy (DOE) labs at Sandia National Labs in Livermore, CA, from which the PI of this proposal (Horstemeyer) worked for 15 years. In fact, Horstemeyer [2012] just released a book entitled "Integrated Computational Materials Engineering (ICME): Using Multiscale Modeling to Invigorate Engineering Design with Science," which thoroughly describes the methodologies for garnering high fidelity simulation solutions in the context of design and manufacturing. It employs an effective hierarchical method for multiscale bridging is the use of thermodynamically constrained internal state variables (ISVs) that can be physically based upon microstructure-property relations. It is a top-down approach, meaning the ISVs exist at the macroscale but reach down to various subscales to receive pertinent information. Essentially, the subscale simulations can be used to determine the appropriate ISV or the attributes of the ISV, like its rate, temperature dependence, etc. Several versions of this particular ISV model were implemented into many of the DOE simulation codes: Dyna, Pronto, Adagio, CTH, JAC/JAS, TAHOE, and several others of the SIERRA codes. It was also implemented into industrial codes such as ABAQUS-Implicit, ABAQUS-Explicit, ESI Pamcrash, ESI-Pamstamp, MSC codes, and Altair's Hyper-Extrude.

The viscoplasticity model formulated by Bammann et al. [1993] coupled with the damage model of Horstemeyer [2012], called DMG-plasticity model, is used in this work to describe the nonlinear response of the material behavior. The thermo-viscoplastic constitutive equations are developed in the framework of the classical thermodynamics of irreversible processes with internal state variables (ISVs). Based upon a multiplicative decomposition of the deformation gradient into elastic and plastics parts, and assuming linear isotropic elasticity with respect to the natural configuration associated with this decomposition, the assumption of linear elasticity can be written:

$$\widehat{\boldsymbol{\sigma}} = \boldsymbol{C}\colon \boldsymbol{D}^{\boldsymbol{e}} = \lambda\, tr(\boldsymbol{D}^{\boldsymbol{e}})\mathbf{1} + 2\mu \boldsymbol{D}^{\boldsymbol{e}} \tag{1}$$

where, $\boldsymbol{D}$ is the elastic strain rate tensor, $\boldsymbol{C}$ is the elastic stiffness, and λ and μ the elastic Lame constants, and the Cauchy stress tensor $\boldsymbol{\sigma}$ is convected with the elasctic spin $\boldsymbol{W}^{\boldsymbol{e}}$ as:

$$\widehat{\boldsymbol{\sigma}} = \dot{\boldsymbol{\sigma}} - \boldsymbol{W}^{\boldsymbol{e}}\boldsymbol{\sigma} + \boldsymbol{\sigma}\,\boldsymbol{W}^{\boldsymbol{e}}. \tag{2}$$

Decomposing the total strain rate $\boldsymbol{D}$ into elastic and plastic parts, the elastic relation can also be written

$$\dot{\boldsymbol{\sigma}} = \boldsymbol{C}\colon (\boldsymbol{D} - \boldsymbol{D}^{\boldsymbol{p}}). \tag{3}$$

The plastic flow rule is defined by the hyperbolic sine functional form

$$\boldsymbol{D^p} = \begin{cases} f(T)\sinh\left[\dfrac{|\boldsymbol{s}-\boldsymbol{\alpha}| - [\kappa - Y(T)](1-\phi)}{(1-\phi)V(T)}\right]\boldsymbol{n} & if\ |\boldsymbol{s}-\boldsymbol{\alpha}| - \kappa - Y(T) \geq 0 \\ 0 & if\ |\boldsymbol{s}-\boldsymbol{\alpha}| - \kappa - Y(T) < 0 \end{cases}, \quad (4)$$

where ϕ is the total damage and $\boldsymbol{n}$ the plastic normal tensor defined by

$$\boldsymbol{n} = \frac{3}{2}\frac{\boldsymbol{s}-\boldsymbol{\alpha}}{|\boldsymbol{s}-\boldsymbol{\alpha}|}. \quad (5)$$

$Y(T)$, $f(T)$ and $V(T)$ are temperature dependent functions and are related to yielding with an Arrhenius-type temperature dependence. The function $Y(T)$ is the rate-independent yield stress, the function $f(T)$ determines when the rate-dependence affects initial yielding, and the function $V(T)$ determines the magnitude of rate-dependence on yielding.

The definition of this plastic flow rule leads to a Mises type yield function defined by

$$f = |\boldsymbol{s}-\boldsymbol{\alpha}| - (1-\phi)\left\{\kappa - Y(T) - V(T)\sinh^{-1}\left[\frac{\dot{\lambda}_p}{f(T)}\right]\right\} = 0. \quad (6)$$

The evolution of the plasticity internal state variables is prescribed in the hardening-minus recovery format. The hardening may be defined as the increase in yield stress due to plastic deformation. For hardening materials, the yield surface will evolve in space in one of three ways:

- The first form of yield surface evolution is called isotropic hardening, κ, which reflects the effect of the global dislocation density. For isotropic hardening, the yield surface grows in size while the center remains at a fixed point in stress space (Figure 6).
- The second form of yield surface evolution is called kinematic hardening, $\boldsymbol{\alpha}$, also called Bauschinger effect (Figure 6), which reflects the effect of anisotropic dislocation density. For kinematic hardening, the center of the yield surface translates in stress space, while the size remains fixed. For both isotropic and kinematic hardening, the orientation of the yield surface remains fixed.
- The third type of yield surface evolution is called mixed hardening where both isotropic and kinematic hardening characteristics are evident. For mixed hardening, the orientation (not considered here) of the yield surface may also change as well.

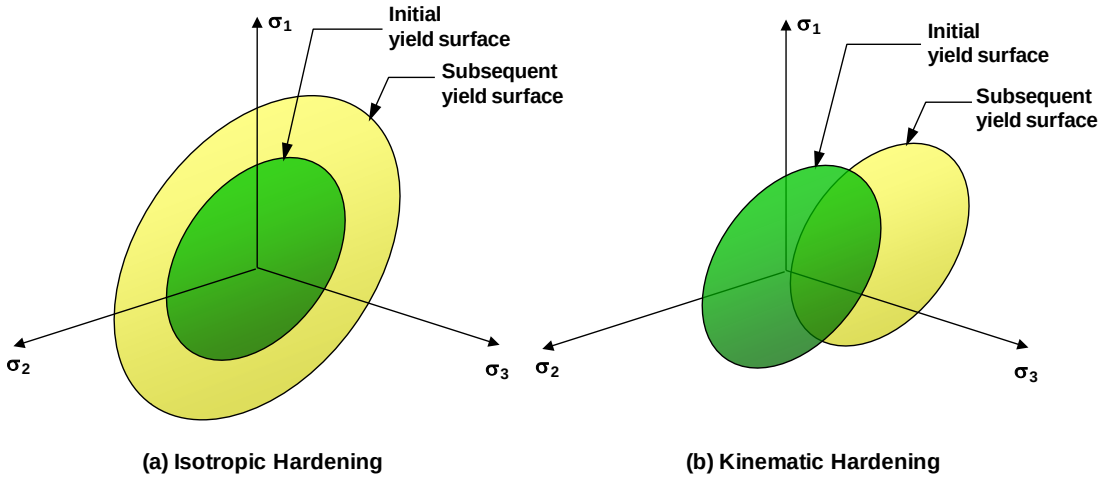

Figure 6. Evolution of the yield surface in case
of (a) isotropic hardening and (b) kinematic hardening.

Although isotropic hardening is the most common form of yield surface evolution assumed in finite element models for metal forming simulation, it is not necessarily the most accurate. The mixed hardening model is most likely the most accurate of the three models. The kinematic hardening internal state variable $\boldsymbol{\alpha}$, representing the directional hardening, is define by the evolution equation

$$\dot{\boldsymbol{\alpha}} = h(T)\boldsymbol{D}^p - \left[r_d(T)\bar{d}_p + r_s(T)\right]\|\boldsymbol{\alpha}\|\boldsymbol{\alpha} \tag{7}$$

and the isotropic hardening κ by

$$\dot{\kappa} = H(T)\bar{d}_p - \left[R_d(T)\,\bar{d}_p + R_s(T)\right]\kappa^2 \tag{8}$$

where

$$\bar{d}_p = \sqrt{\frac{2}{3}\boldsymbol{D}^p{:}\,\boldsymbol{D}^p} \quad \text{and} \quad \|\boldsymbol{\alpha}\| = \sqrt{\frac{3}{2}\boldsymbol{\alpha}{:}\,\boldsymbol{\alpha}}\,. \tag{9}$$

The temperature dependence of the hardening functions $H(T)$ and $h(T)$ should in general be proportional to the temperature dependence of shear modulus. The terms $r_s(T)$ and $R_s(T)$ are scalar functions describing the diffusion-controlled static or thermal recovery, and $r_d(T)$ and $R_d(T)$ are the functions describing the dynamic recovery. The temperature-dependent functions are defined in Table 1, in which $J_2 = \frac{1}{2}(\boldsymbol{\sigma}' - \boldsymbol{\alpha}')^2$ and $J_3 = \frac{1}{2}(\boldsymbol{\sigma}' - \boldsymbol{\alpha}')^3$. The deviatoric stress $\boldsymbol{\sigma}'$ is expressed in indicial notation as $\sigma'_{ij} = \sigma_{ij} - I_1$ with $I_1 = \frac{1}{3}\sigma_{ii}$.

The damage variable ϕ represents the damage fraction of material within a continuum element. The mechanical properties of a material depend upon the amount and type of microdefects within its structure. Deformation changes these microdefects, and when the number of microdefects accumulates, damage is said to have grown. The process of ductile fracture of most metals and alloys occurs mainly due to the void nucleation, growth and finally coalescence into a micro-crack (Figure 7). If the extent of void growth up to fracture

is small, it is possible to ignore its effects on the constitutive equations. However, a realistic model on ductile fracture prediction must include void nucleation, void growth and a condition for void coalescence.

Table 1. Material parameters C_i for the viscoplasticity model.

Mechanism	Description	Term Definition
Yield Stress	Rate-Independent Yield Stress	$Y(T) = \frac{C_3(1+\tanh[C_{19}(C_{20}-T)])}{2(C_{21}+\exp[-C_4/T])}$
	Magnitude of Rate-Dependence on yielding	$V(T) = C_1 \exp[-C_2/T]$
	Rate-Dependence on Initial Yielding	$f(T) = C_5 \exp[-C_6/T]$
Kinematic Hardening	Modulus	$h(T) = C_9\left[1 + C_{20}\left(\frac{4}{27} - \frac{J_3^2}{J_2'^3}\right)\right] - C_{10}T$
	Dynamic Recovery	$r_d(T) = C_7\left[1 + C_{19}\left(\frac{4}{27} - \frac{J_3^2}{J_2^3}\right)\right]\exp[-C_8/T]$
	Static Recovery	$r_s(T) = C_{11}\exp[-C_{12}/T]$
Isotropic Hardening	Modulus	$H(T) = C_{15}\left[1 + C_{22}\left(\frac{4}{27} - \frac{J_3^2}{J_2^3}\right)\right] - C_{16}T$
	Dynamic Recovery	$R_d(T) = C_{13}\left[1 + C_{21}\left(\frac{4}{27} - \frac{J_3^2}{J_2^3}\right)\right]\exp[-C_{14}/T]$
	Static Recovery	$R_s(T) = C_{17}\exp[-C_{18}/T]$

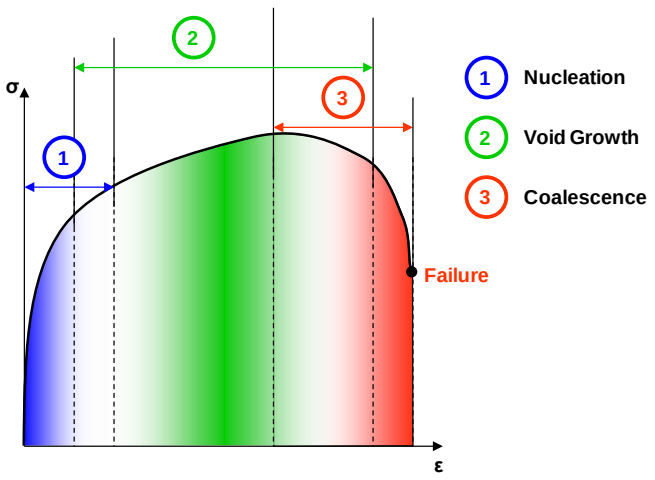

Figure 7. Sequences in a ductile fracture mechanism.

The damage progression is divided into void nucleation η and growth v from silicon particles and from pores. The coalescence c is introduced to reflect pore-pore interactions and silicon-pore interactions as expressed in

$$\phi = (\eta v + \phi_{pore})C \tag{10}$$

The void nucleation rule of Horstemeyer and Gokhale [1999] is used to model the results from the experimental data under compression, tension, and torsion. The integrated form of the void nucleation rate equation is given by

$$\eta(t) = C_{coeff} \exp\left(\frac{\varepsilon(t) d^{1/2}}{K_{IC} d f^{1/3}} \left\{ a\left[\frac{4}{27} - \frac{J_3^2}{J_2^3}\right] + b\frac{J_3}{J^{3/2}} + c\left\|\frac{I_1}{\sqrt{J_2}}\right\| \right\}\right) \exp\left(\frac{C_{T\eta}}{T}\right) \tag{11}$$

where $\eta(t)$ is the void nucleation density, $\varepsilon(t)$ is the strain at time t, C_{coeff} is a material constant. T is temperature in the absolute scale, and $C_{T\eta}$ is the temperature dependent material constant determined from experiments. The volume fraction of the second phase material is *f*, the average silicon particle size is *d*, and the bulk fracture toughness is K_{IC}. The material parameters *a, b*, and *c* relate to the volume fraction of nucleation events arising from local microstresses in the material. These constants are determined experimentally from tension, compression, and torsion tests in which the number density of void sites is measured at different strain levels. The stress state dependence (compression, tension, and torsion) on damage evolution is captured in Eq. (6.17) by using the three stress invariants denoted by I_1, J_2, and J_3, respectively [Horstemeyer and Gokhale, 1999].

A crucial feature in determining the damage state, besides nucleation of voids, is void growth. Several void growth models are considered. The first one by McClintock [1968] is given in terms of the void radius as

$$\dot{v} = \frac{\sqrt{3}R_0}{2(1-n)}\left[\sinh\left(\sqrt{3}(1-n)\frac{\sqrt{2}I_1}{3\sqrt{J_2}}\right)\right]\bar{d}_p \tag{12}$$

where the void volume grows as the strain and/or stress triaxiality increases. The material constant *n* is related to the strain hardening exponent and is determined from the tension tests. R_0 is taken to be the initial radius of the voids. Void growth for large pore in this context is that by Cocks and Ashby [1980] given in terms of the void volume fraction rate

$$\dot{\phi}_{pore} = \left[\frac{1}{(1-v)^{1/m}} - (1-v)\right]\sinh\left[\frac{2(2-m)}{2+m}\frac{\sqrt{2}I_1}{3\sqrt{J_2}}\right]\bar{d}_p \tag{13}$$

where $m = V(T)/Y(T)$ is the strain rate sensitivity.

The void coalescence is the joining of voids either at the microscale or macroscale and has been observed to occur by two main mechanisms: natural coalescence where two neighboring voids grow together until they join as one, and void sheet mechanism where a localized shear band occurs between neighboring voids. Coalescence arises naturally with the multiplicative relation between the nucleation and growth terms:

$$C = \left[C_{D_1} + C_{D_2}\eta v\right]\left(\frac{DCS_0}{DCS}\right)^z (TC_{TC}) \quad (14)$$

where DCS_0 and DCS are the initial and current dentritic cell sizes, and C_{TC} is the temperature dependent material constant determined from experiments. The parameters C_{D_1}, C_{D_2} and z are material constants.

4.5 METAMODEL DEVELOPMENT

When high-fidelity FE simulations are combined with numerical design optimization, the computational cost tends to drastically increase; moreover, when gradient-based optimization methods are used, solution accuracy and convergence are jeopardized if the response characteristics that appear in the objective or constraint functions are highly non-linear and noisy. To avoid these difficulties, the computationally expensive simulations are replaced with low-cost surrogate models (metamodels) that can provide sufficiently accurate approximation of the response values at a considerably shorter timeframe. The goal of metamodeling is to replace an exact response function $f(x)$ found using a high-fidelity simulation with an approximate analytic function $f'(x)$ with $x = \{x_1, x_2, \dots, x_n\}^T$representing an n-dimensional vector of input variables. Metamodeling techniques aim at regression and/or interpolation fitting of the response of interest based on the exact or measured values of response at the specified training (observation) points that are selected using one of many design and analysis of computer experiments techniques. Each design point represents a unique combination of input variables.

A number of metamodel types may be used to fit the data source of finite element responses generated in Task 2. The types may be categorized according to the mathematical method of construction. Example methods include:

- Interpolation methods
    - Radial basis functions (RBF)
    - Artificial neural networks (ANN)
- Regression methods
    - Polynomial response surface (PRS)
    - Support vector regression (SVR)
    - Multivariate adaptive regression splines
    - Gaussian process (GP)
- Hybrids
    - Kriging (KR; interpolation + regression)
    - Ensemble (ENS; weighted contributions from several methods)

The quality metric of a metamodel is specified by a measure which identifies the algorithm to estimate the metric and the error function to be utilized. Some of the measure types are: Cross validation, Validation set, Min-max, and Sample error.

Depending on the measure type, the error function may be: Average absolute error, Root mean square error, and Maximum relative error. Multiple measures may be combined to build a metamodel that satisfies multiple objectives.

Each metamodel type has a set of parameters that control the complexity of the metamodel. The process of finding a "good" set of parameters, with respect to the chosen measure, is referred to as metamodel parameter optimization or calibration. Some of the optimization methods that may be employed depending on the metamodel types are: least-squares optimization, genetic algorithm, simulated annealing, pattern search optimization, branch and bound, etc.

The inputs to Task 3: Metamodel Development are the results of finite element simulations of the tube manufacturing process being modeled using ISV theory in ABAQUS (Task 2), and the costs associated with the process (from PTC). These comprise the data source for the process from which various metamodels for the process may be constructed. The finite element simulations require very long running times, and only a few results are available for Task 3. Thus, datasets were generated to mimic the possible results of the finite element simulations.

The first output of Task 3 is software to automatically construct codes for metamodels from the data source. The software is capable of scoring each metamodel it constructs, in order to facilitate automated selection or informed manual selection by the software end-user, of metamodels for best fits to the data available in the data source.

The second output of Task 3 is software that utilizes the metamodel to predict the mechanical properties of tubes and to estimate the cost of producing the tubes. This software is intended to end-users at PTC.

Task 3 adopted MATLAB (The MathWorks Inc., 2010) and Surrogate Modeling Toolbox v.7.0.2 (D. Gorissen, L. De Tommasi, K. Crombecq, T. Dhaene, 2009) as the tools for building metamodels and development of software for end-users. These two tools combined provide all the functionalities required for Task 3.

The following are the procedures performed under Task 3:

1. Generate simulated datasets describing the microstructure-process-property relationships in selected tube manufacturing processes
2. Develop *scripts* to derive a metamodel for forming process data, using SUMO.
3. Develop prototype software implementing 'microstructure-process-property-cost' relationships, using MATLAB-Simulink and the forming process metamodel
    a. Code#1 – implements the relation *(Sheet microstructure, Forming process settings) → (Tube properties, Cost)*
    b. Code#2 – implements the relation *(Sheet microstructure, Desired tube properties) → (Forming process settings, Cost)*
4. Test the scripts and codes on simulated forming data.
5. Conduct live demonstration of the codes at PTC.

5 RESULTS AND DISCUSSION

5.1 MICROSTRUCTURE ANALYSIS

Optical microscopy revealed a ferrite-pearlite microstructure throughout all the 1010 steel samples. This is consistent with observations found in literature (Benscoter and Bramfitt 2004). The State 1 material had uniform grain sizes throughout the thickness of the steel plate in each of the three orientations. Figure 8 seen below shows the ferrite-pearlite microstructure of the State 1 material in the rolling direction.

(a)

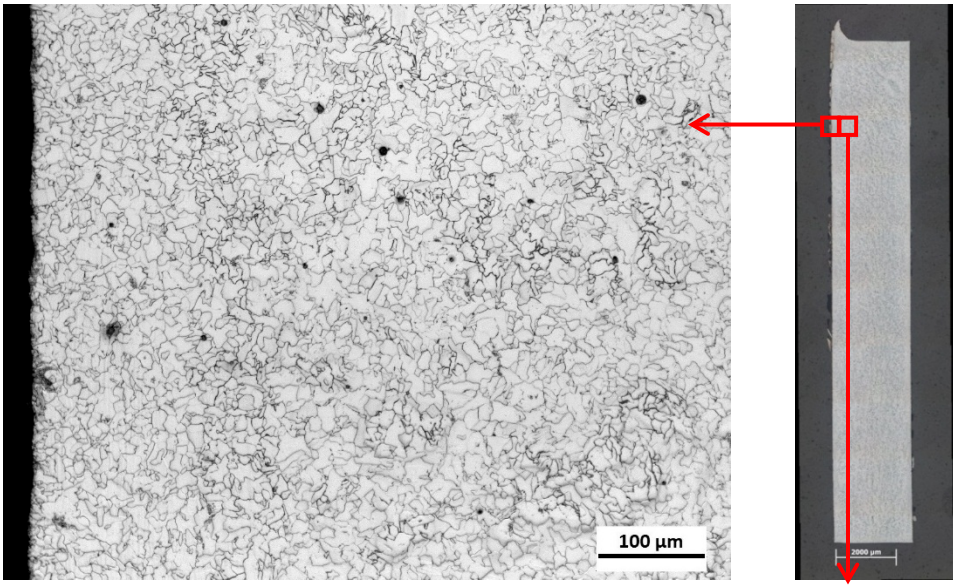

(b)

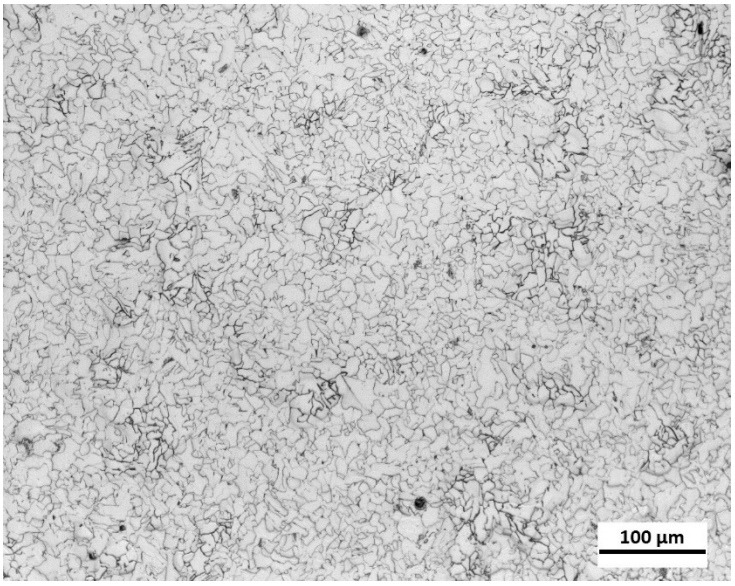

Figure 8. State 1 (Steel Coil) material, rolling direction, optical microcopy; (a) uniform ferrite-pearlite microstructure on plate edge (b) grain size consistent through plate thickness.

A significant amount of cold working is induced when the rollers form the steel into a tubular shape. This is easily seen when looking at the pre-welded edge of the State 2 material. In Figure 9 elongated grains are seen on the free edge of the cross section orientation sample. This is the point on the steel coil material that experiences the most strain in the forming process. The thin elongated grains are evidence of the extreme cold working and residual stress that is still in the tube after encountering the rollers. Other than the elongation of grains on the free edge, however, the microstructure is very similar to that seen in the State 1 material.

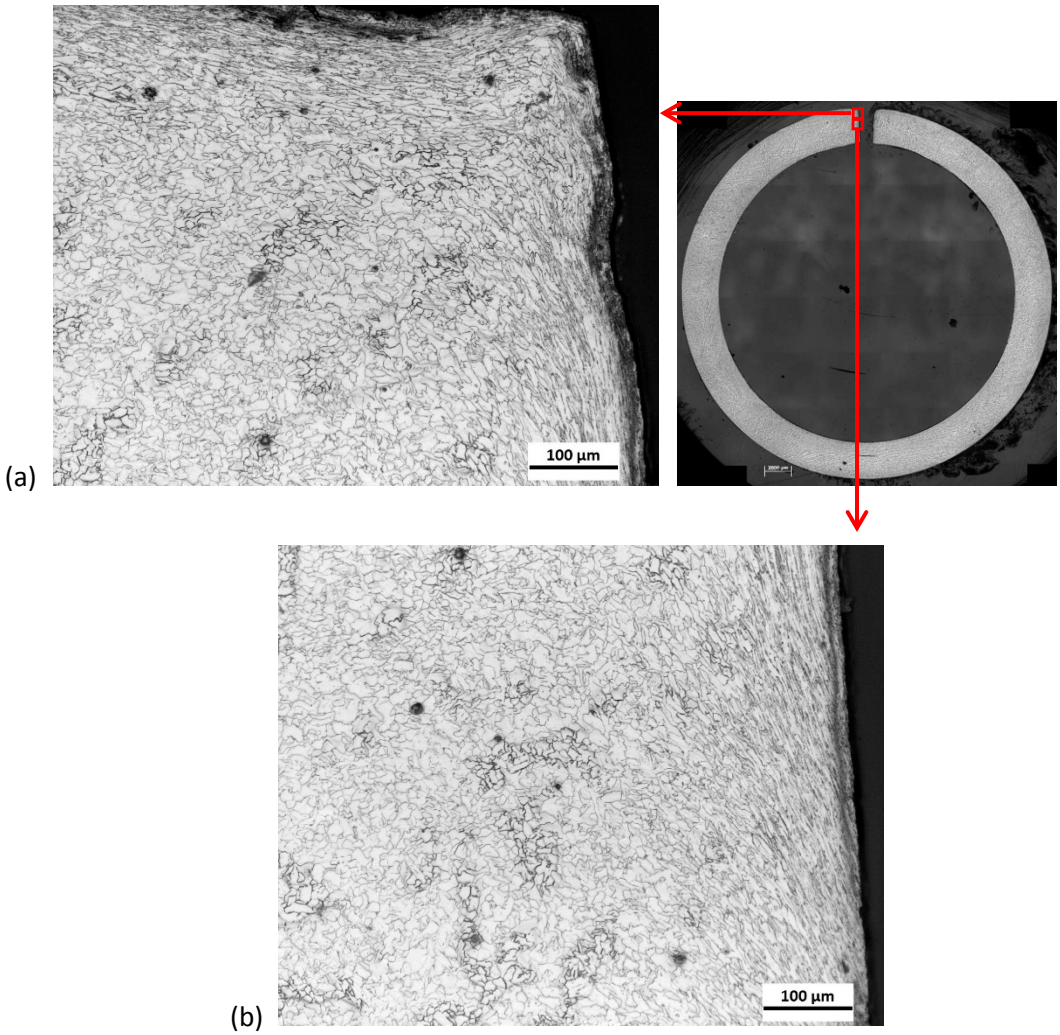

Figure 9. State 2 (After Forming) optical microscopy; (a) elongated grains at top corner of pre-welded tube edge (b) elongated grains continue along the entire edge.

The grain structure of the State 3 material is similar to that of the previous state, except for at the weld. The rapid increase and then decrease of heat exposure due to the induction welding of the steel causes a phase change to occur in the heat affected zone (HAZ). It appears that the microstructure in the HAZ consists of bainite "pockets" dispersed throughout the ferrite grains. Figure 10 shows the microstructure through the HAZ. The bainite present in the HAZ affects the mechanical properties. There is a localized brittle

area at the weld location which will have high strength and toughness, but the malleability of the tube in this location will decrease dramatically (Davis 1998).

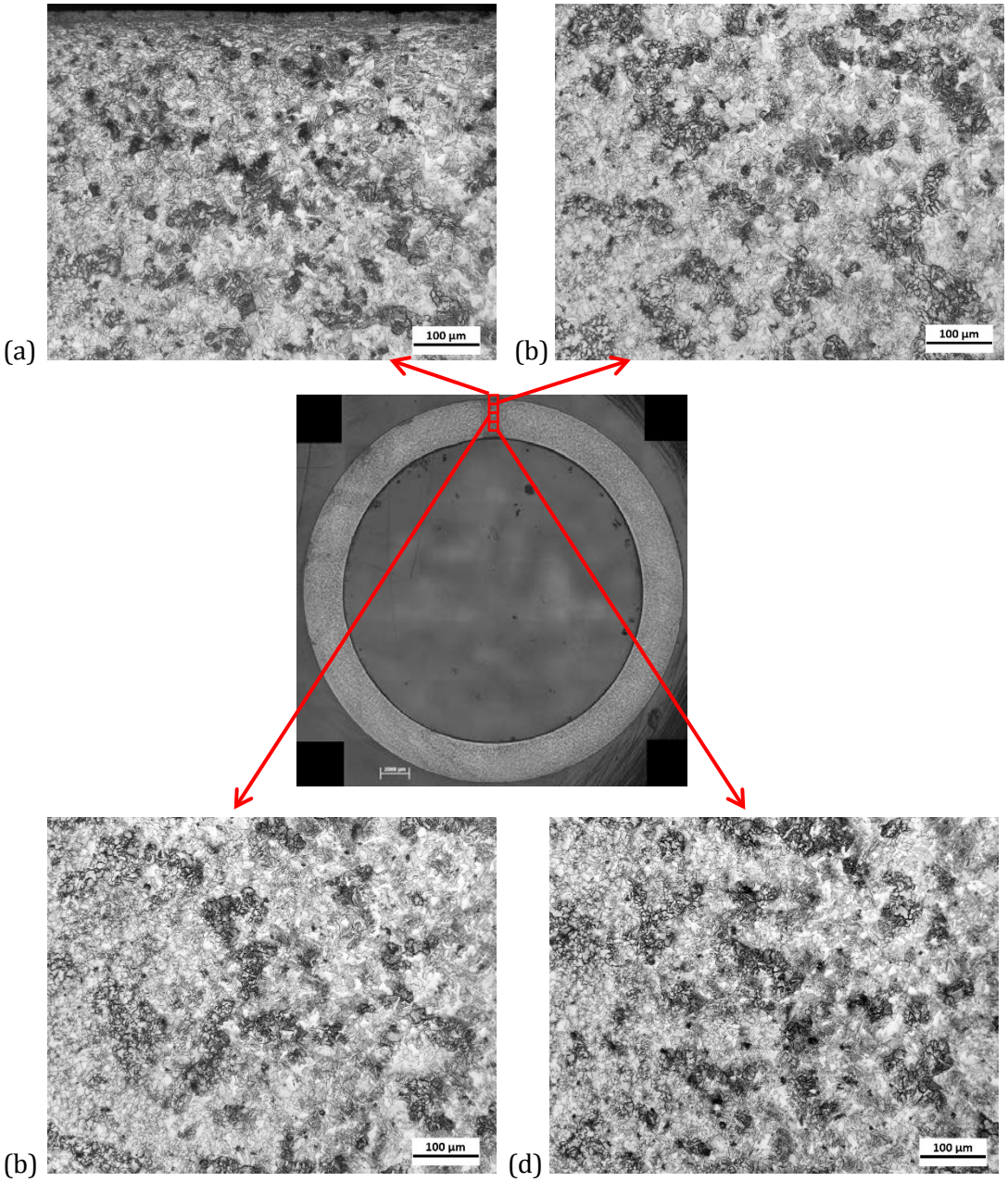

Figure 10. State 3 (After Sizing) optical microscopy, cross section orientation; change in phase from ferrite-pearlite to ferrite-bainite in HAZ.

Figure 11 is a representative of the ferrite-pearlite microstructure present in the transverse orientation far from the weld. The microstructure seems to be unaffected by the high heat experienced during the welding process.

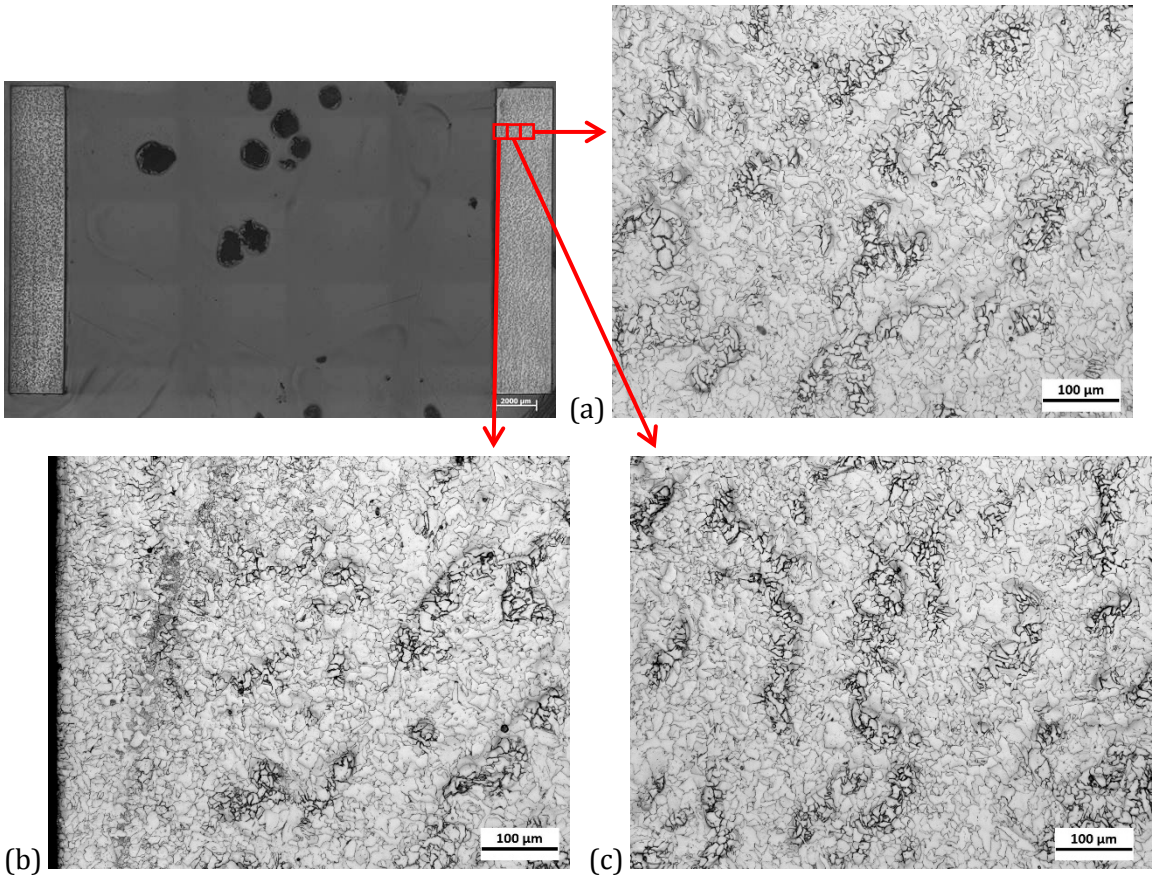

Figure 11. State 3 (After Sizing) optical microscopy, rolling orientation; ferrite-pearlite microstructure throughout thickness of the tube.

After the sizing process, the tube goes through a heat treatment process. During the heat treatment process the furnace heats the steel past the A_3 temperature as seen on an iron-carbon phase diagram. This relieves the residual stresses and causes the grains to grow and become more uniform. This is easily seen in the optical microscope images. One thing to point out is that the grains are significantly larger on the outer radius of the tube. This is due to an effect known as decarburization. This occurs when atoms of carbon, combined with oxygen present in the atmosphere, take a gaseous form of carbon monoxide (Mercier, Lesage, Decoopman, and Chicot, D. 2006). If decarburization is significant it can modify mechanical properties of the steel, decreasing fatigue life. To combat this effect, the steel is cooled in an inert atmosphere consisting of 10% hydrogen and 90% nitrogen. Figure 12 shows the increase in the ferrite grain size, showing a uniform microstructure except for the decarburization zone at the OD of the tube.

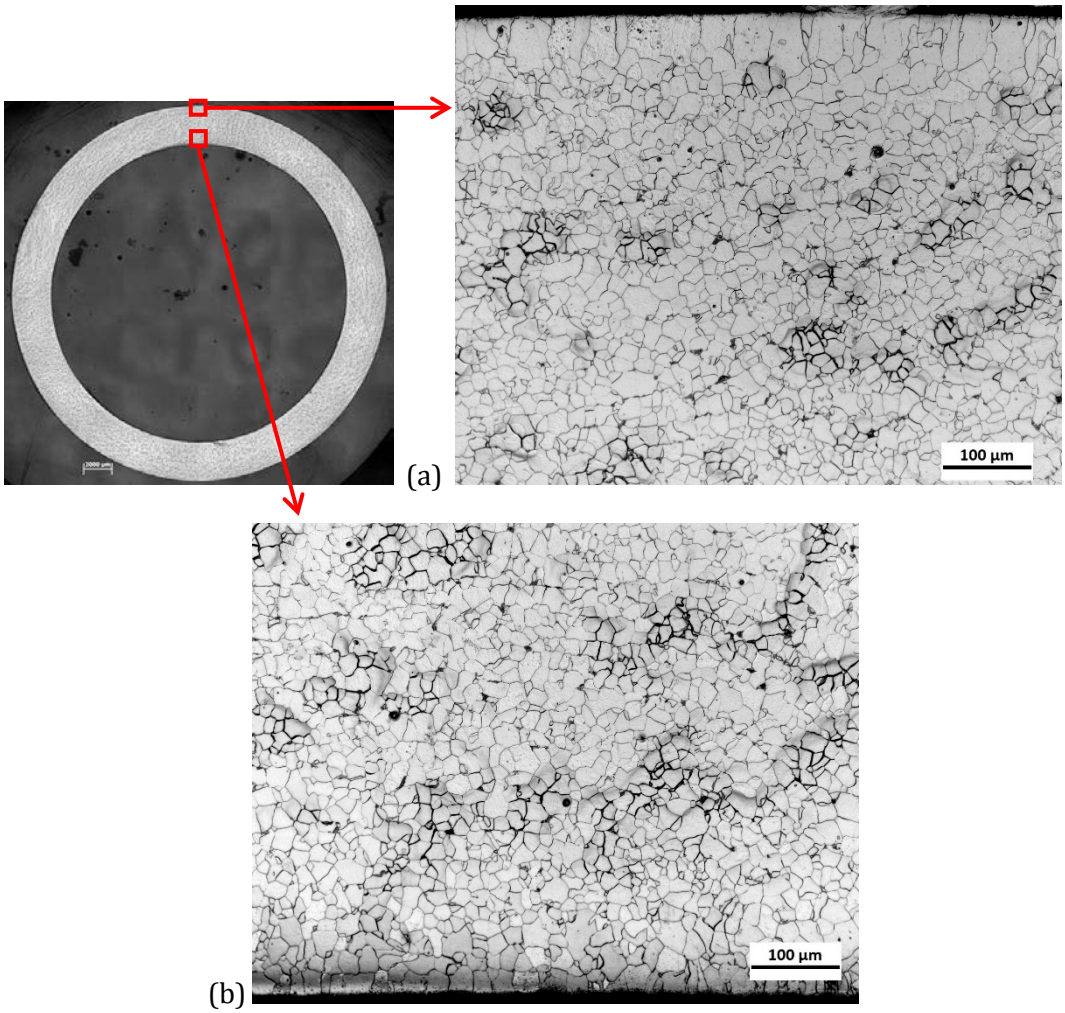

Figure 12. State 4 (After 1st Normalization) optical microscopy, cross section orientation; (a) localized decarburization at tube OD (b) uniform grain size throughout the rest of the tube thickness.

After the tube exits draw bench #1 a slight decrease in the ferrite grain size can be seen from the previous state in the cross section orientation (Figure 13). This is attributed the amount of cold work present in the drawing process.

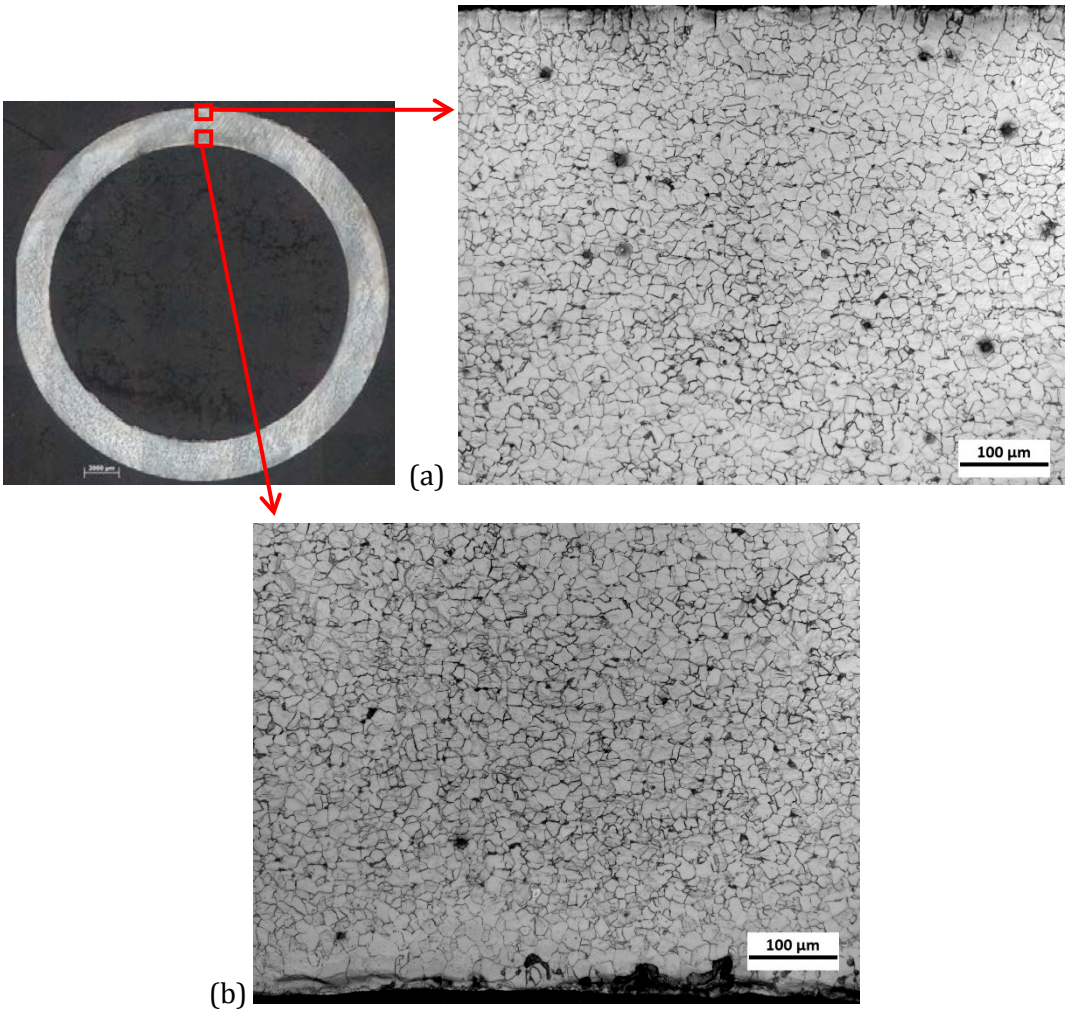

Figure 13. State 5 (After Draw Bench #1) optical microscopy, cross section orientation; reduced grain size from State 4 with larger ferrite grains at ID and OD of tube.

The more significant microstructure change can be seen in the transverse and normal to transverse orientations. The grains are elongated parallel to the rolling direction. This is to be expected due to the high stress placed on the tube by the die normal to the tube cross section. Figure 14 below shows the elongated grains seen in the tube in the transverse orientation after the first draw bench.

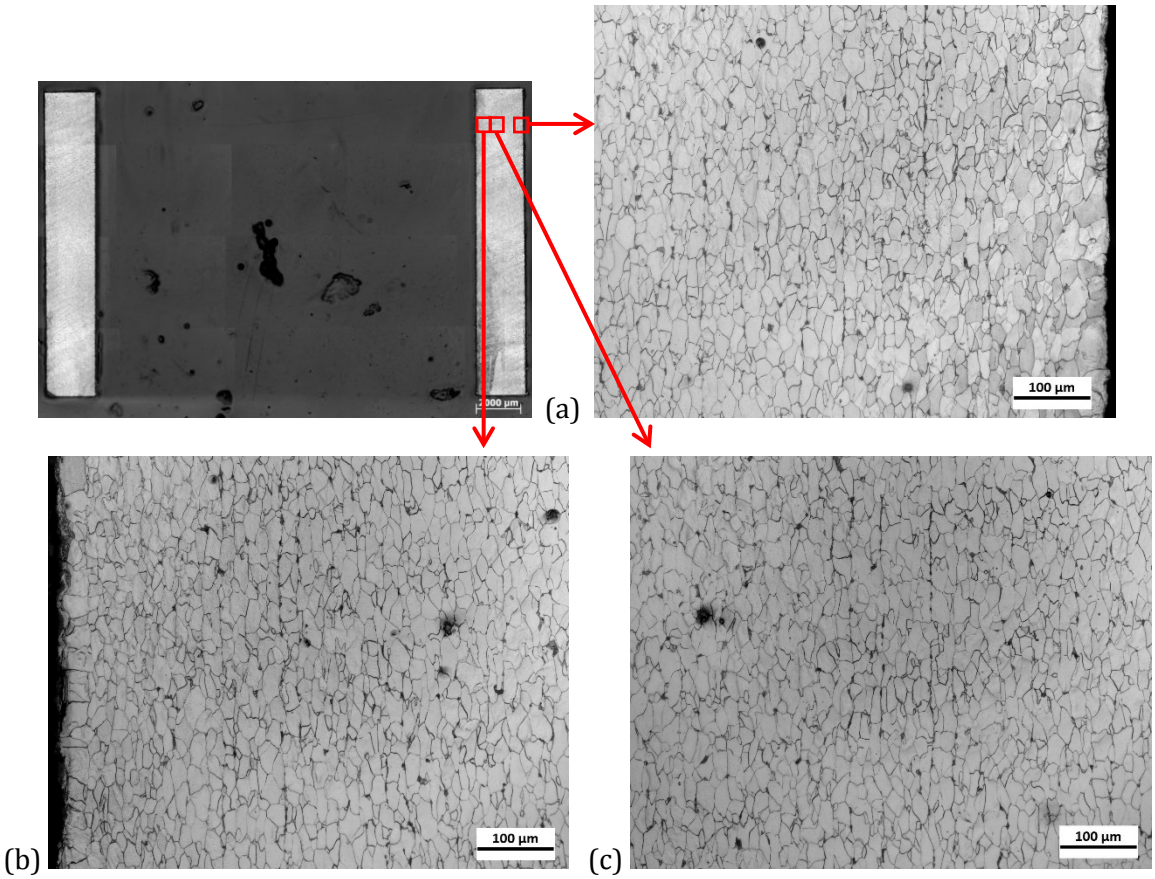

Figure 14. State 5 (After Draw Bench #1) optical microscopy, transverse orientation; (a) (b) elongated ferrite grains, larger at ID and OD of tube (c) elongated uniform ferrite grain size in tube center.

At State 6 there is a definite decrease in grain size in the cross section orientation. It also appears that the grains are slightly elongated perpendicular to the radius of the tube, the most elongated grains being at the inner diameter. This could be attributed to there being no mandrel to control the inner diameter during this drawing process. The grains are free to deform radially towards the ID of the tube. Figure 15 shows the reduction in grain size and the radial elongation experienced in the cross section orientation.

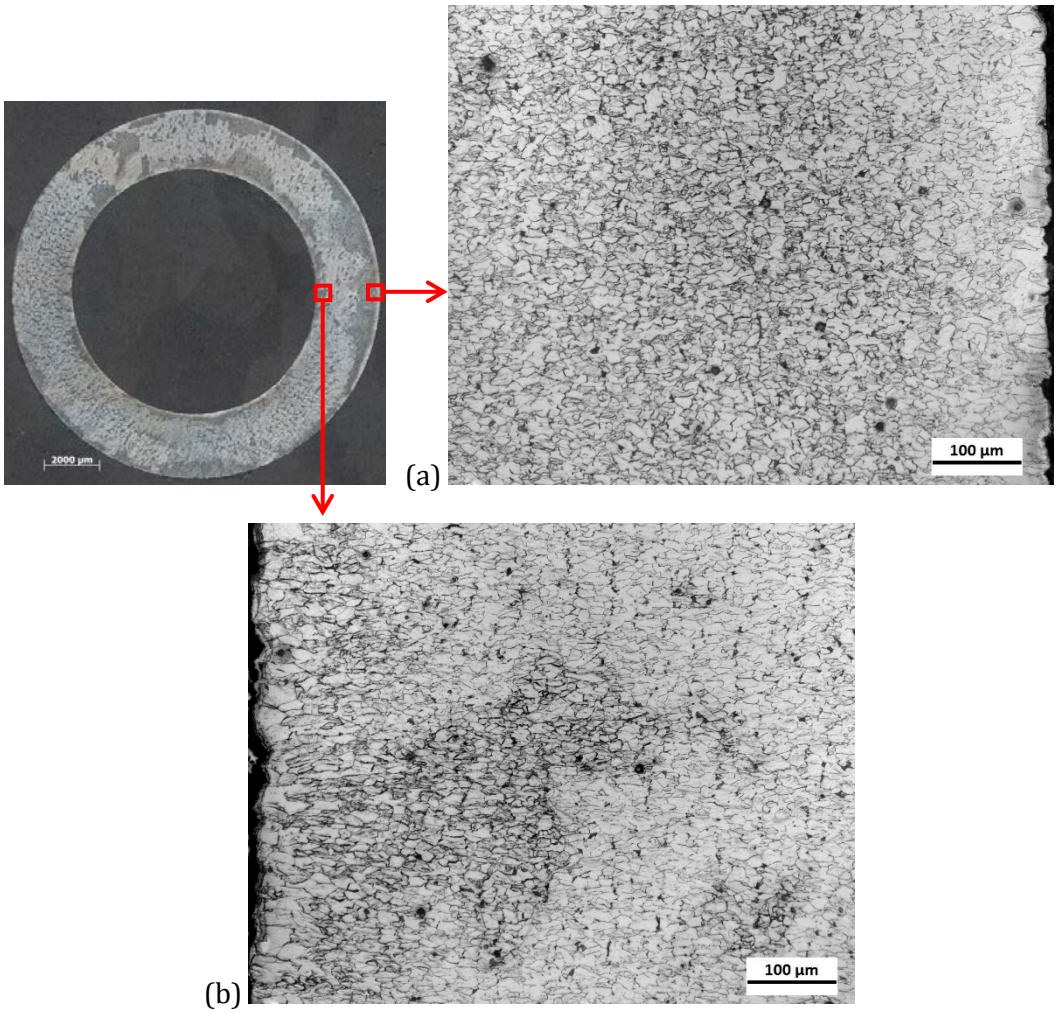

Figure 15. State 6 (After Draw Bench #2) optical microscopy, cross section orientation; (a) grain size reduction compared to State 5 with radially elongated grains and (b) grains become even more elongated at tube ID.

In the transverse and normal to transverse orientations, there is an even more drastic elongation of grains parallel to the drawing direction, as seen in Figure 16. This is caused by the cold working experienced by the drastic change in the tube OD.

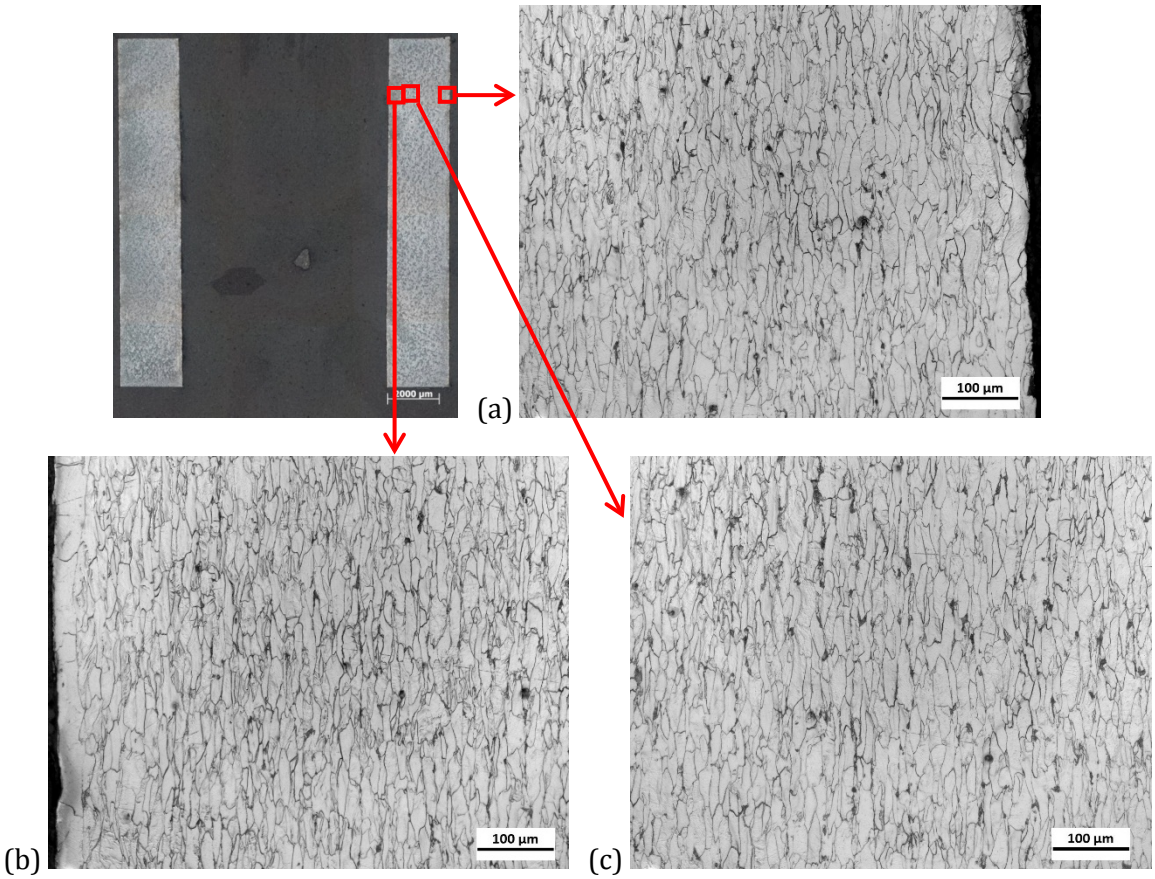

Figure 16. State 6 (After Draw Bench #2) optical microscopy, transverse orientation; drastic elongation of ferrite grain diameter with larger grains at ID and OD of tube.

At State 7, again the heat treatment has caused the grains to grow significantly and become more uniform. This is what to expect after a full anneal. The grains are larger at the outer diameter of the tube. This can be seen in all of the specimen orientations. This increase in grain size is beneficial for ductility but detrimental for the toughness of the material. Figure 17 shows the State 7 tube microstructure. This is the final state of the tube before it is shipped to the customer.

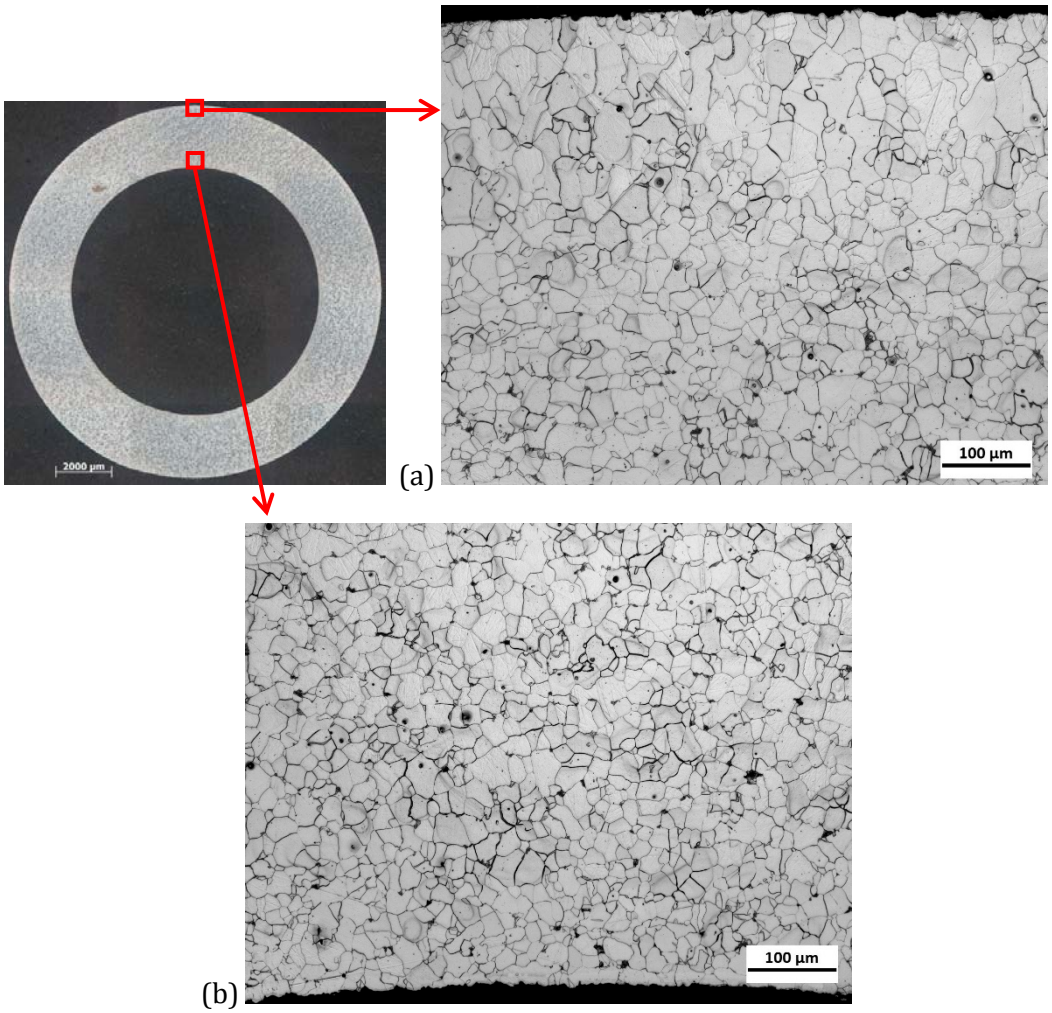

Figure 17. State 7 After Final Anneal optical microscopy, cross section orientation; larger, more uniform grain size except for even larger grains at OD contributed to decarburization.

5.2 TENSILE TEST DATA

The room temperature true stress-true strain curves of the 1010 steel from all of the material states are shown in Figure 18. They are typical of most low carbon dual-phase steels; deforming linear-elastically until yield and then experiencing work hardening until the ultimate tensile strength (UTS) is reached. There are, however, drastic differences in the tensile properties of the materials when comparing all seven states. The State 4 and State 7 material have similar work hardening rates and UTS; both having the lowest stength when compared to the other material states. This is to be expected because State 4 and State 7 occur immediately after a full anneal. They consist of a microstructure of large, uniform ferrite grains that promote ductility but reduce material strength. The State 1 material has a slightly higher UTS than that of material from States 4 and 7. This is consistent with microstructure observations because the State 1 grain size is smaller than both the post annealed grain sizes. The forming and sizing processes increase the strength of the material, as seen by the State 2 and State 3 curves, respectfully. The elongation to

failure, however, decreases dramatically. The effect the cold working has on the steel can be seen most by the State 6 and State 7 curves. There is a striking increase in the strength of the material, with relatively no work hardening seen in the steel.

Another material attribute that can be drawn from the stress-strain behavior is the presents of Luders bands in the deformation of the steel. The yield point elongation seen most easily in the stress-strain curves from States 1, 4, and 7 occurs when a discrete band of deformed metal appears at a stress concentration such as a fillet. The band then propagates along the length of the specimen, causing the yield point elongation. Usually there are multiple bands that form at approximately 45° to the tensile axis (Dieter 1988).

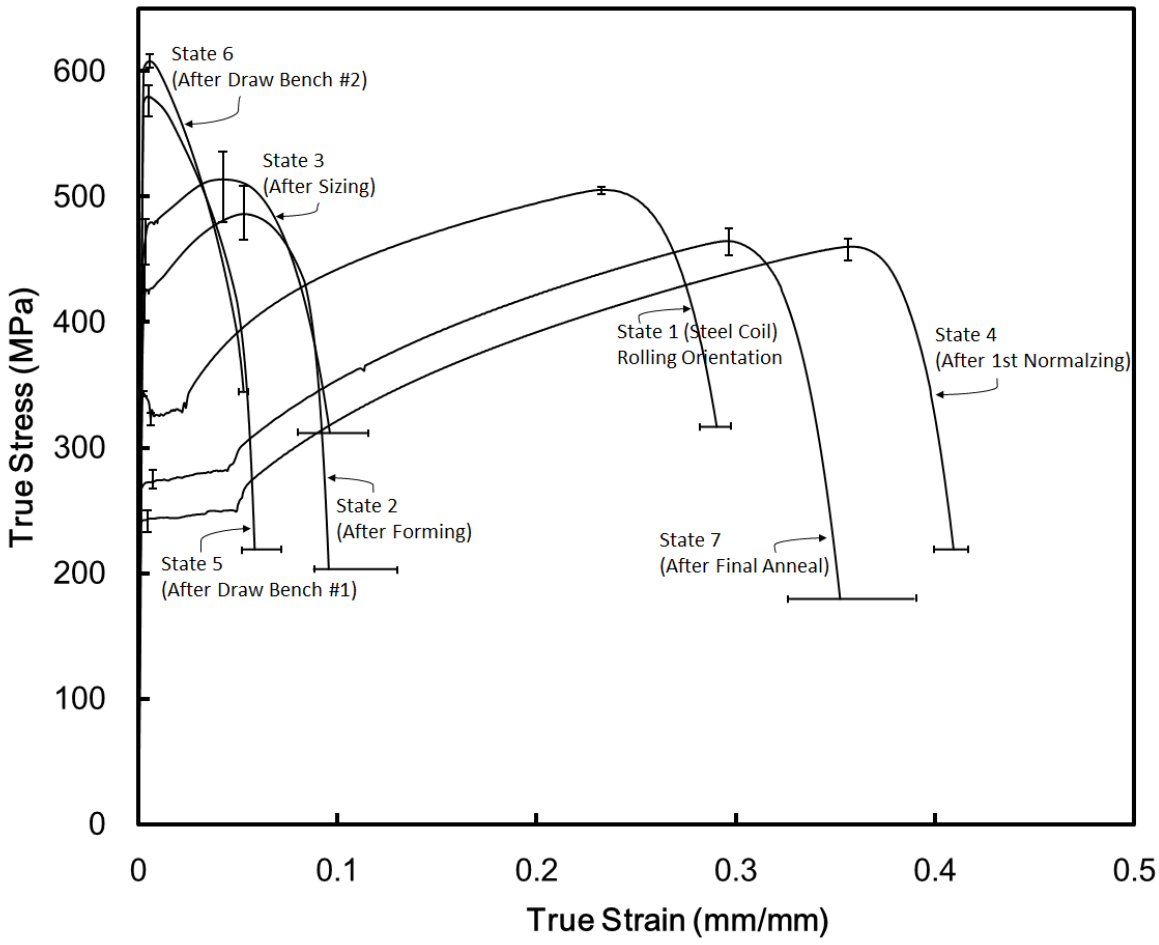

Figure 18. True stress-strain behavior of 1010 steel from all material states.

A summary of the tensile data can is shown in Table 2. The first three columns are the yield strength, the UTS, and the elongation to failure, respectfully. The last three columns show a change in these values from the previous material state.

Table 2. Summary of tensile properties and comparison to previous state

	σ_y (MPa)	σ_{ult} (MPa)	ε_F (mm/mm)	$\Delta\sigma_y$ (MPa)	$\Delta\sigma_{ult}$ (MPa)	$\Delta\varepsilon_F$ (mm/mm)
State 1 (Steel Coil)	352	498	0.257	n/a	n/a	n/a
State 2 (After Forming)	426	486	0.096	+74	-12	-0.161
State 3 (After Sizing)	467	514	0.096	+41	+28	+0
State 4 (After 1st Normalization)	243	460	0.409	-224	-54	+0.313
State 5 (After Draw Bench #1)	580	580	0.058	+337	+120	-0.351
State 6 (After Draw Bench #2)	608	608	0.053	+28	+28	-0.005
State 7 (After Final Anneal)	273	465	0.352	-335	-143	+0.299

5.3 ISV PLASTICITY-DAMAGE MODEL CALIBRATION AND VALIDATION

Using the DMG-Fit software developed at CAVS, the ISV material set of constants was fitted to the stress-strain experimental curves for different temperatures and strain rates. Figure 19 shows the fitting of the 1010 steel material constants for tensile tests conducted at room temperature (298K) and high temperature (623K).

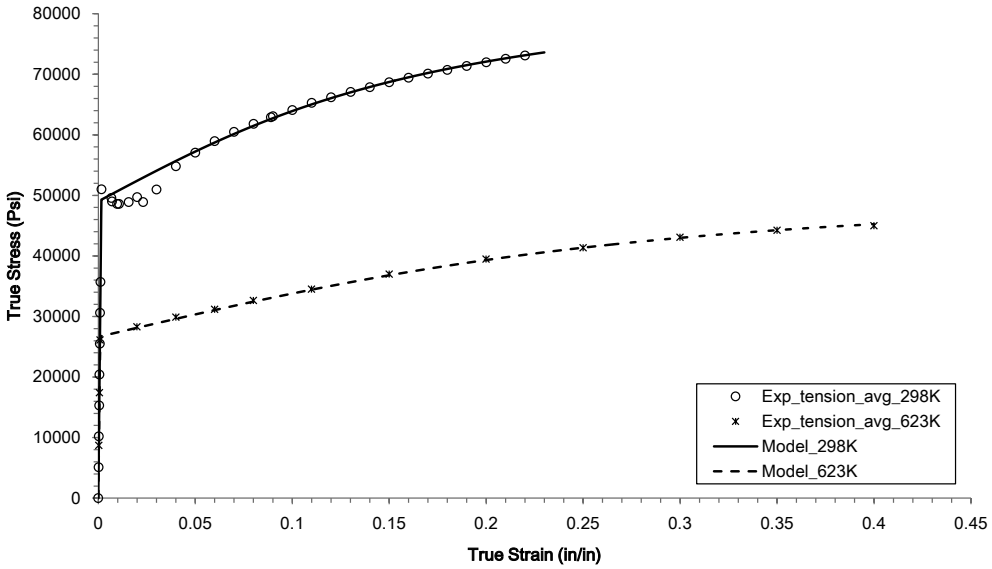

Figure 19. State 1 (raw sheet material) stress-strain calibration of MSU DMG-ISV model with experimental data.

5.4 LARGE SCALE FINITE ELEMENT SIMULATIONS IN HPC ENVIRONMENT

The different main steps of the tube forming of a 1010 steel sheet were simulated using the finite element method in a High Performance Computing (HPC) environment. The finite element is currently the best numerical technique to accurately model metal forming

processes; however they often require a considerable amount of CPU time, even in a HPC environment with multiprocessors. The cost of CPU time can be even more expensive if 3D solid elements and 3D contact are needed to predict the correct deformation of the tube as it is the case for the forming process in which a couple of dozen of contact surfaces are involved. Therefore, the objective of these simulations is to provide a numerical database that will be used in the metamodeling framework, in which the numerical results will be interpolated to obtain a predicted solution in a timely manner for different processing conditions.

The tube forming involves several different processing steps, such as forming, welding, normalizing, sizing, tubing, etc., that are sequentially modeled in eventual separate steps. In the Plymouth Tube facility, tubes are physically cut at the end of some steps before being transferred to the next step. Therefore it is completely realistic to simulate processing steps separately with different boundary conditions and initial conditions. Extremely long tubes are formed under steady-state conditions, therefore only a short length of the tube is necessary to obtain a finite element prediction, which has the advantage to decrease the CPU time.

In order to link each step, the material history must be captured and carried to the next step as initial conditions with the objective of predicting the mechanical properties at the end of the tube forming process. To simulate a single step, the following tasks must be defined:

- Mesh definition of the with 3D solid elements or shell elements of the ;
- Definition of rigid surfaces using analytical or discrete surfaces;
- Boundary conditions and contact interaction (velocity, temperature profile, contact friction coefficient);
- ISV material constants of the microstructure-plasticity DMG model;
- Initial material solution (ISV initialization).

At the end of each step, the ISV material solution through is homogenized and used as initial material condition in the following step. In other words, the isotropic and kinematic hardenings are initialized based to the material solution of the previous state. The material behavior is described using the ISV constitutive model for microstructure-plasticity, implemented in the user material subroutine VUMAT of Abaqus/Explicit.

5.4.1 SIMULATIONS OF FORMING PROCESS

In this pipe forming simulation, the blank material is traveling through several rollers that will force the flat sheet to bend in order to form a tube before getting welded. All rollers were assumed rigid and represented by analytical surfaces that piloted by reference points. The coefficient of friction was approximated to 0.1 and the boundary conditions were set to:

- Rollers: free to rotate on only one axis (z-axis or y-axis);
- Material Velocity: 30 inch/sec (0.76 m/sec).

The ISV material constants were set to represent the 1010 steel material (see Figure 20) and large deformations were considered (nonlinear geometry). The objective of the forming

simulation was to predict the material solution at the end of the sequence and compare the stress-strain curve with experimental data.

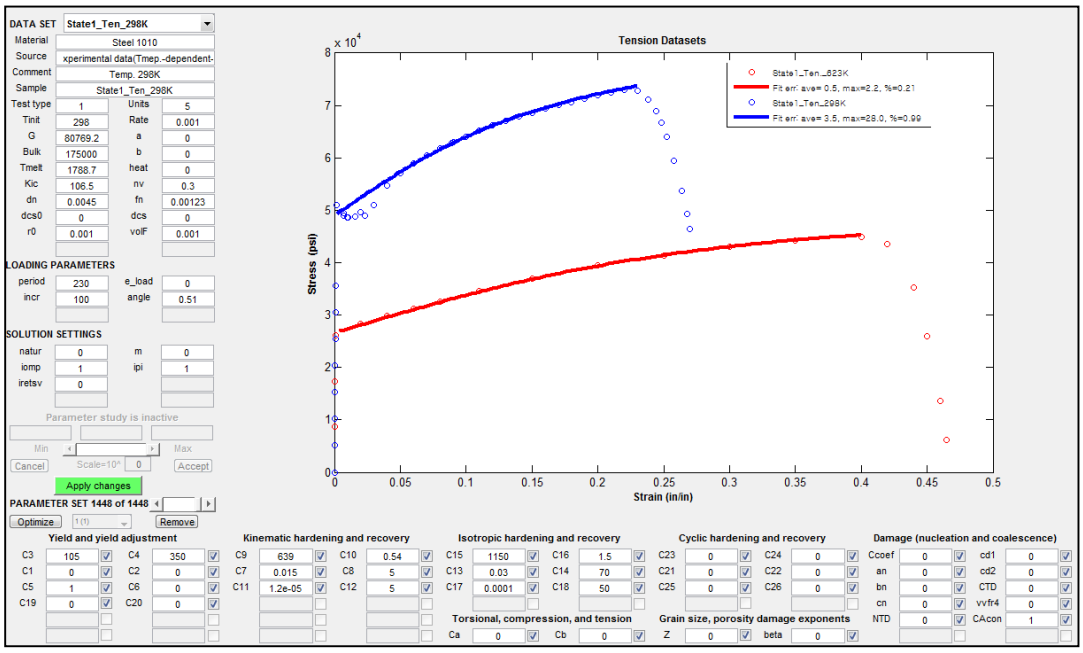

Figure 20. Calibration of the ISV material constants to describe the 1010 steel material response in tension.

Shell elements and continuum solid elements from the Abaqus/Explicit element library were used and tested to obtain best results. The continuum (solid) elements are the most comprehensive of the element libraries in Abaqus. The elements are available in Abaqus/Explicit only with reduced integration, which have the advantage to not exhibit shear locking in their evaluation of the element strain energy that eliminates the shear locking phenomenon, however multiple elements through the thickness are needed to model the bending response accurately. Regarding shell elements, two types are available in Abaqus: conventional shell elements and continuum shell elements. Conventional shell elements discretize a reference surface by defining the element's planar dimensions, its surface normal, its initial curvature, and its thickness. Continuum shell elements, on the other hand, resemble three-dimensional solid elements in that they discretize an entire three-dimensional body yet are formulated so that their kinematic and constitutive behavior is similar to conventional shell element (Abaqus reference). Two shell elements and one solid element were used and tested in this forming simulation, which are the following:

- S4R shell element, a 4-node general-purpose shell, reduced integration with hourglass control, finite membrane strains;
- SC8R continuum shell element, a 8-node hexahedron, general-purpose, finite membrane strains;
- C3D8R solid element, a 8-node linear brick, reduced integration with hourglass control.

Several simulations were performed to determine the best elements in terms of both solution accuracy and CPU times. The S4R shell element is very CPU inexpensive and robust, which makes it suitable for a wide range of applications. This shell element is used to model structures in which one dimension (the thickness) is significantly smaller than the other dimensions and the stresses in the thickness direction are negligible. Continuum shell elements SC8R behave similarly to conventional shell elements and, therefore, can be used effectively for modeling slender structures dominated by bending behavior. The CPU time with these shell elements is very minimal because only one element is needed through the thickness direction. However, both of these shell elements were not able to correctly capture the large bending during the tubing forming process due to the large thickness of the sheet compared to the other dimension. The solid element C3D8R possesses a single material point due to its reduced integration. This element has also the advantage of eliminating the shear locking phenomenon in its evaluation of the element strain energy eliminates the shear locking phenomenon, however multiple elements through the thickness are needed to model the bending response accurately. In the pipe forming simulation, at least six elements through the thickness were required to correctly capture the bending of the sheet and obtain the correct shape of the tube at the end of the analysis, which considerably increase the CPU time. The finite element analysis had to be restarted several times in the HPC environment in order to complete (each analysis was limited to 48 hour HPC rule).

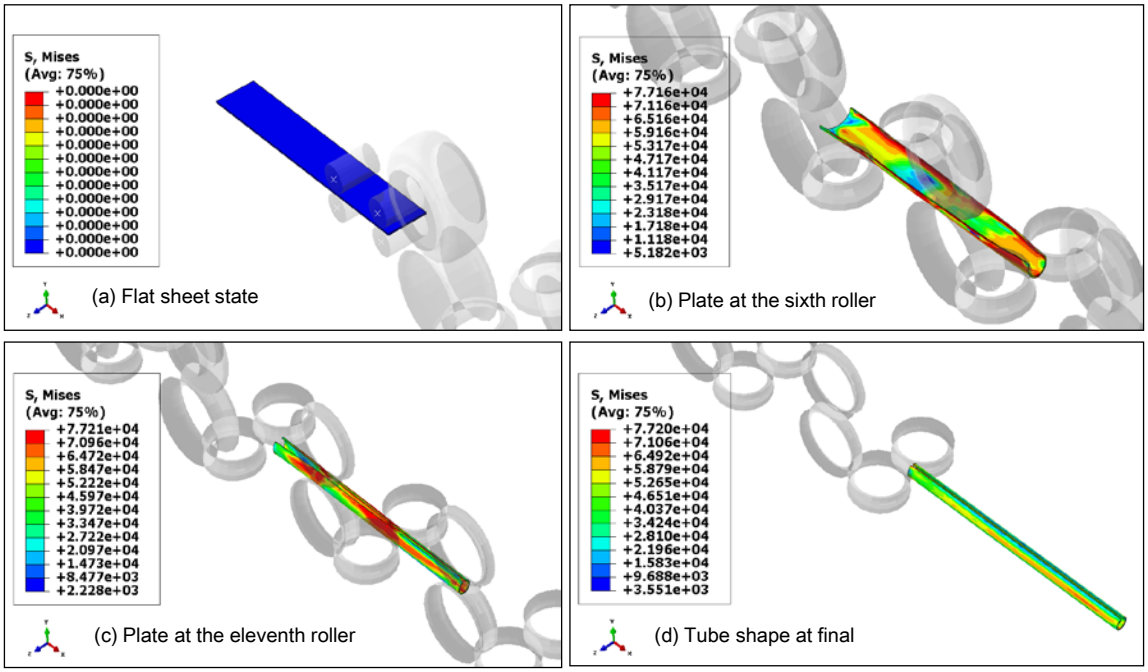

Figure 21. Tube forming simulation showing the von Mises stress (in psi) progression from sheet to tube.

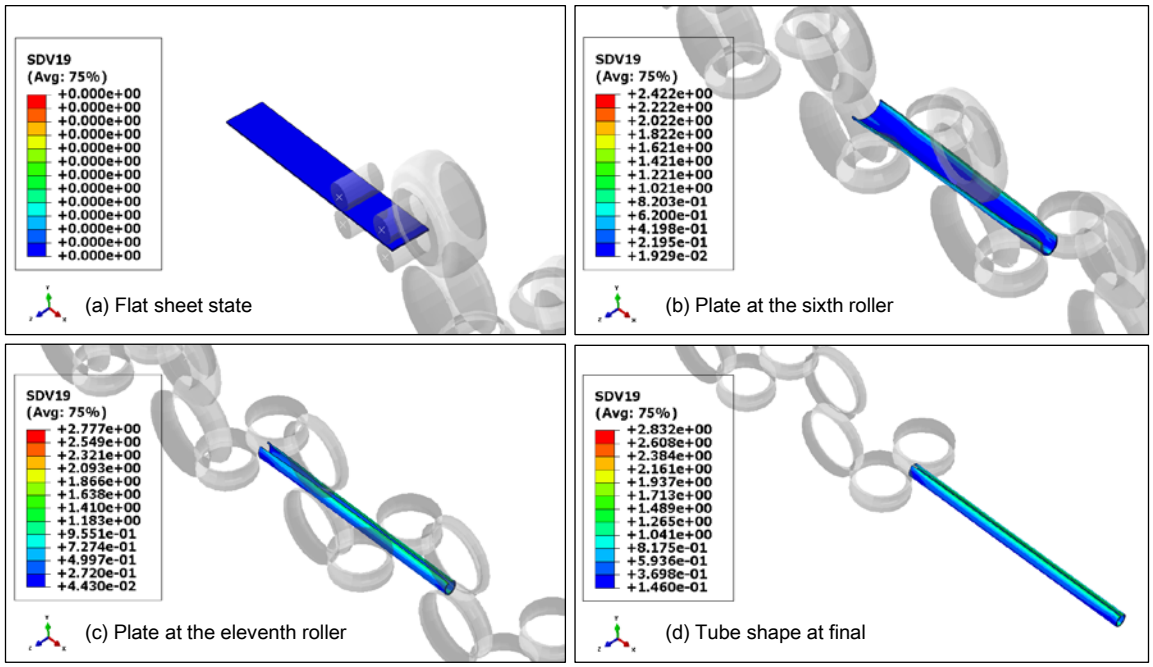

Figure 22. Tube forming simulation showing the von Mises stress progression from sheet to tube.

Figure 21 and Figure 22 show the von Mises stress and plastic equivalent strain, respectively, at different instant of the analysis, starting from the flat sheet state to the final tube shape. We can observe that both the Mises stress and the plastic equivalent strain are not uniform along the circumference of the tube. The thickness increased from 0.108 in at the beginning of the process to 0.118 at the end of the forming process. The simulation was validated by comparing the post-forming stress-strain behavior with experiments (Figure 23). The predicted stress-strain curve was obtained from the finite element tube forming simulation by extracting the average values of isotropic and kinematic hardenings from all elements. The average values were used as initial material conditions in a single representative volume element (RVE), to which tensile boundary conditions were applied. The stress-strain curve in Figure 23 represents the material response of this RVE and it agrees quite well with the post-forming experimental curve.

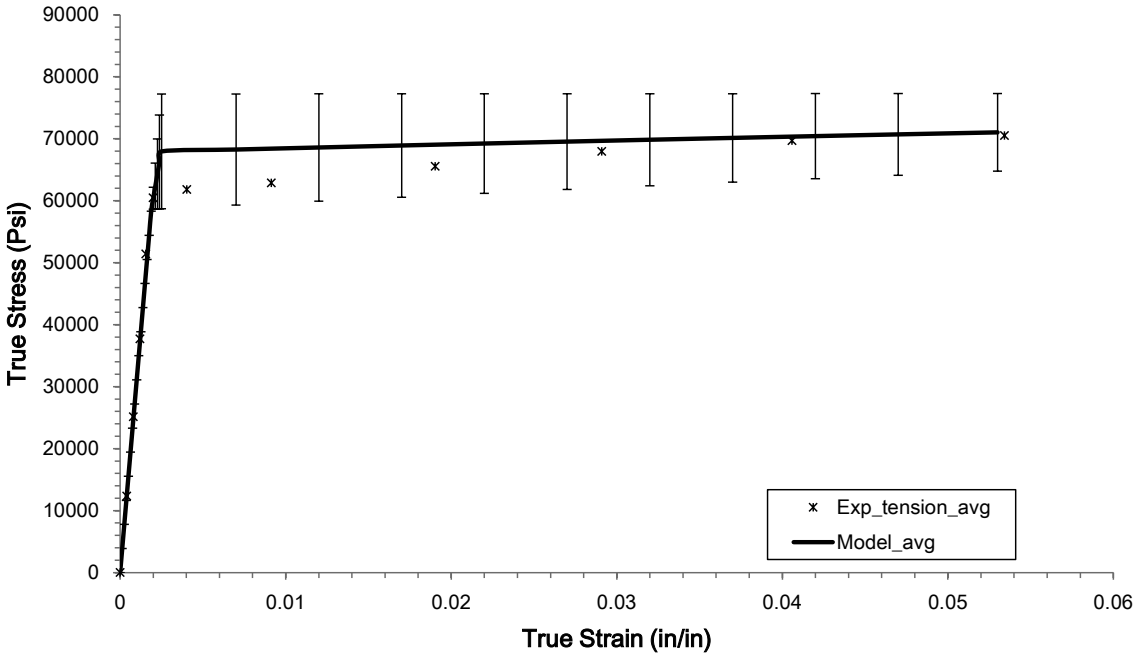

Figure 23. Post-forming (State 2) stress-strain behavior: comparison of the finite element model results and experimental data.

5.4.2 SIMULATIONS OF WELDING PROCESS

In this Phase I, the welding process was reduced to a simple physical joining process where the nodes from both left and right sides were tied using points constraints. The complexity of the welding process and the short term of Phase I did not allow the investigation team to model the microstructural changes during this process. Therefore, the material history at the post-forming state was considered as the initial material solution of the sizing simulation in next section.

5.4.3 SIMULATIONS OF SIZING PROCESS

After welding, the tube is undergoing a sizing process for straightness using several pairs of rollers. Same as in the forming process, rollers were considered rigid and represented in the finite element sizing simulation by analytical rigid surfaces and piloted by reference points in Abaqus/Explicit. The boundary conditions were as following

- Tube: moving in x-direction
- Rollers: free to rotate on only one axis (z-axis or y-axis)
- Material Velocity: 30 inch/sec (0.76 m/sec).

The ISV material constants of the DMG microstructure-plasticity model are identical as in the forming process, and the isotropic and kinematic hardening solutions were uniformly initialized in in the whole tube mesh via the user material subroutine UMAT to capture the material history of post-forming simulation (Figure 23).

In this simulation, a small thickness change was observed throughout the entire step (from 0.102 to 0.103) as the main objective of the sizing process is to straighten the tube. Figure 24 and Figure 25 show the von Mises stress and plastic equivalent strain, respectively, at different instant of the analysis.

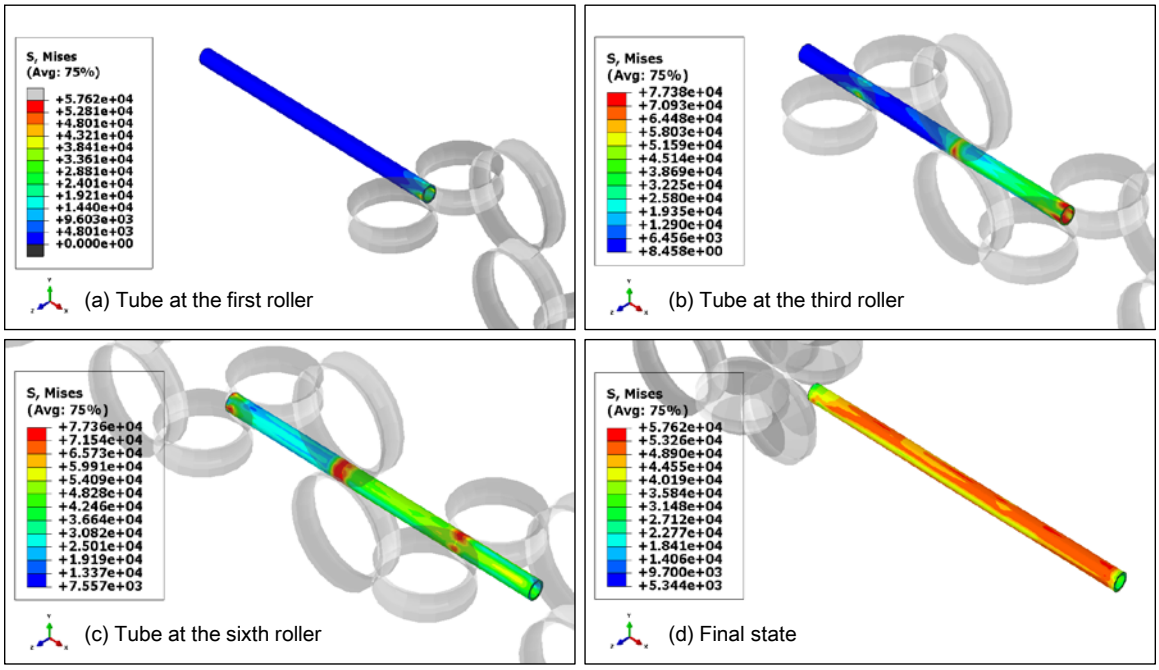

Figure 24. Sizing simulation showing the von Mises stress (in psi) at different instants.

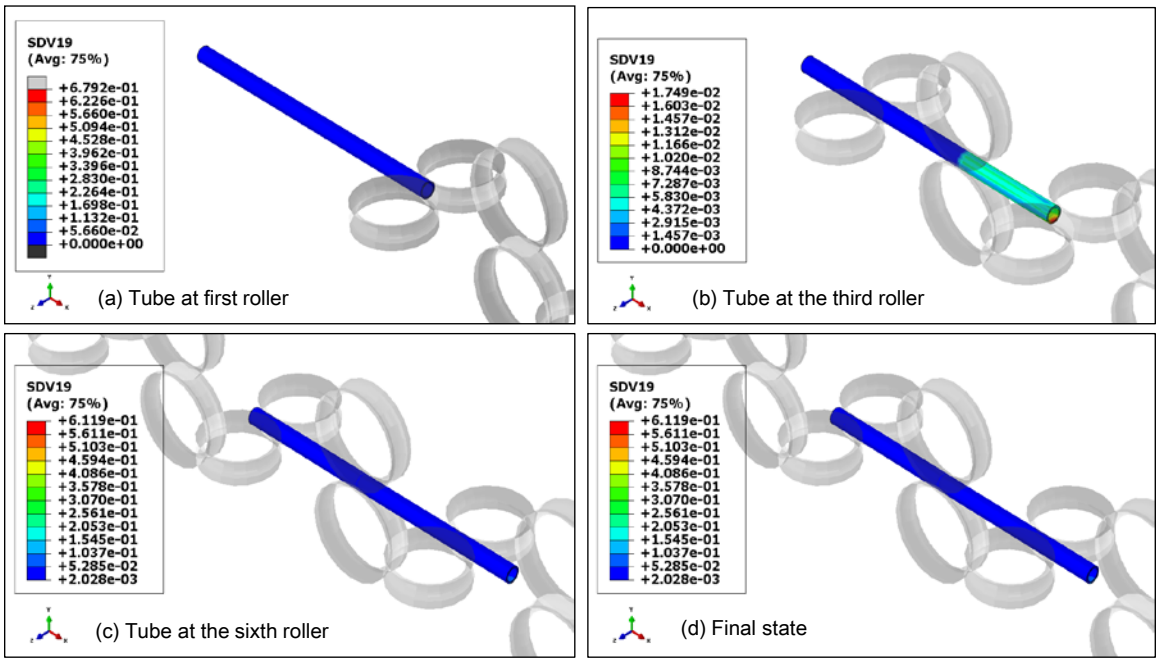

Figure 25. Sizing simulation showing the plastic equivalent strain at different instants

Similarly as in the forming simulation, the predicted stress-strain curve was obtained from the finite element tube forming simulation by extracting the average values of isotropic and

kinematic hardenings from all elements. The stress-strain curve in Figure 26 represents the material response of an RVE with tensile boundary conditions and it agrees quite well with the post-sizing experimental curve.

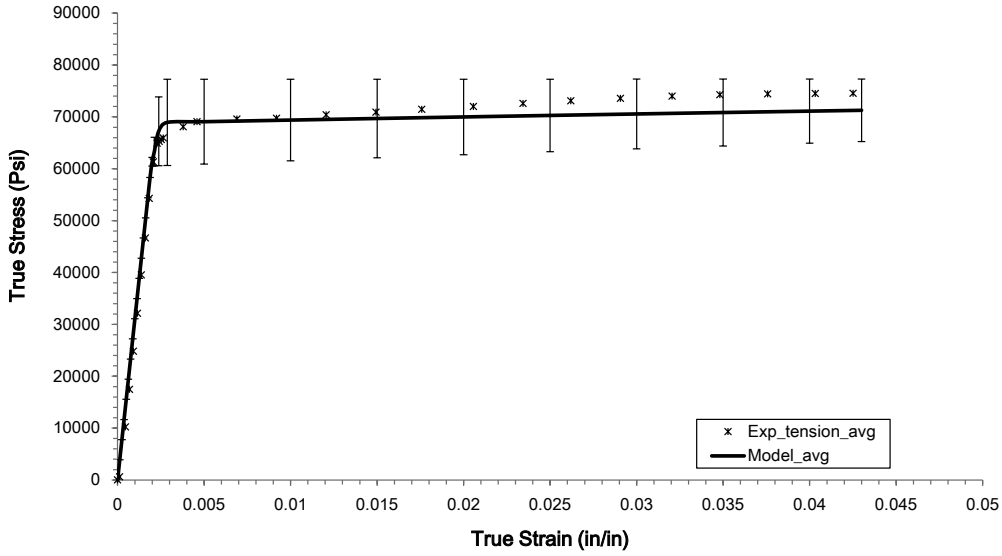

Figure 26. Post-sizing (State 3) stress-strain behavior:t comparison of the finite element model results and experimental data.

5.4.4 SIMULATIONS OF NORMALIZATION PROCESS

In this normalizing simulation, the tube is undergoing a heat treating process to improve to improve the strength and increase the ductile properties of the steel tube. The simulation is performed in Abaqus/Standard using the user material subroutine UMAT, which is equivalent to VUMAT in Abaqus/Explicit. The tube is meshed with C3D8RT coupled temperature-displacement solid elements and the boundary conditions are as following:

- Tube: Stationary
- Heating up to 1200 K – 10 minutes
- Holding to 1200K – 10 minutes
- Cooling down to 298 K – 40 minutes.

In addition to the definition ISV material constants, the following thermal properties of the 1010 steel were also defined:

- Specific heat
- Thermal conductivity
- Coefficient of thermal expansion
- Density

The temperature profile was uniformly applied to all nodes of the tube mesh since it was considered that the diameter dimensions of the tube is very small compared to the furnace used for heat treatment. Most of the deformation that occurred in this normalizing simulation is related to the thermal strain. Since the tube was not constrained at both ends, the stresses are near zero in the tube (Figure 27).

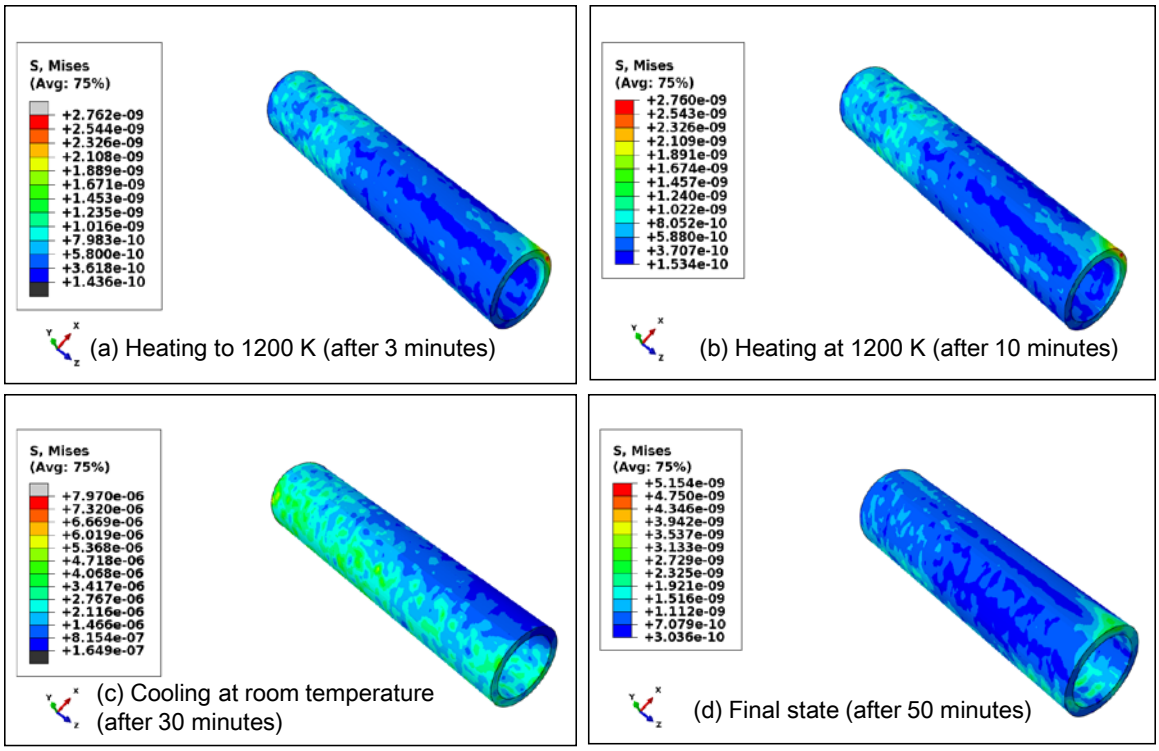

Figure 27. Normalizing simulation showing the von Mises stress (in psi) progression.

The validation of the normalizing step couldn't successfully be performed due to the limitation of the DGM ISV model to capture the stress-strain curve when the sample is subjected to a thermal loading. High temperature during normalizing is changing the microstructure of the material, such as the grain size, and their evolution cannot entirely be captured by the hardening variables. For the continuation of the prediction, the post-normalizing stress-strain was directly fitted with new ISV set of material constants and used for the next steps.

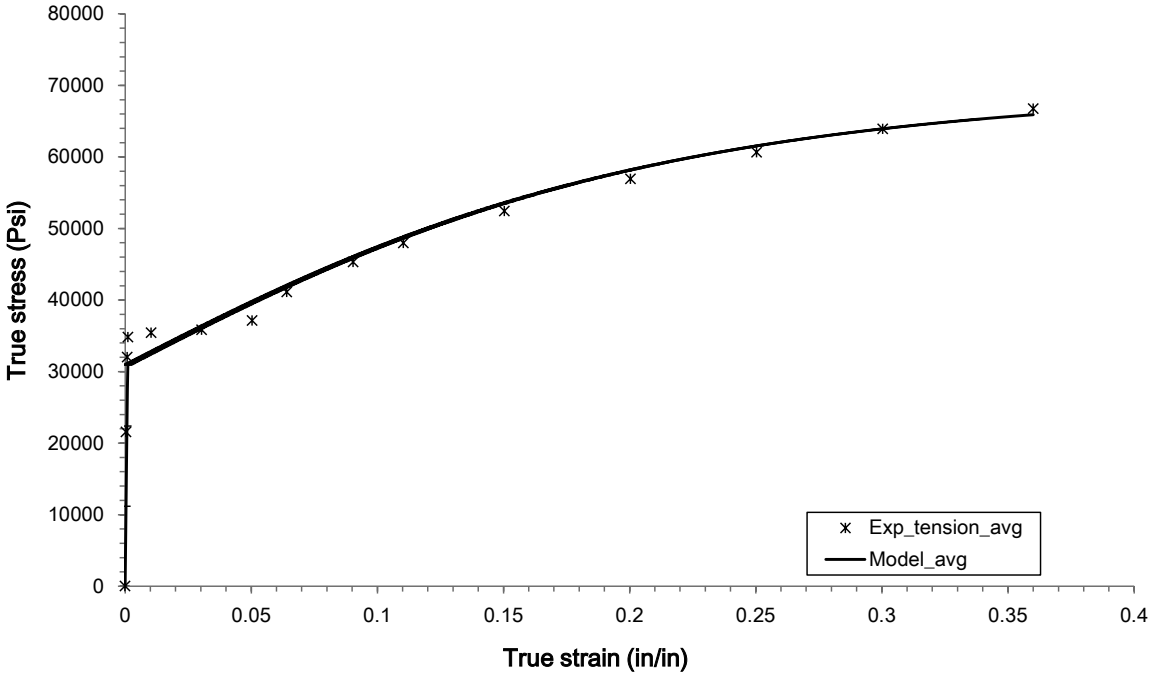

Figure 28. Post-normalization (State 4) stress-strain behavior: comparison of the finite element model results and experimental data.

5.4.5 SIMULATIONS OF DRAWING PROCESSES

The objective of tube drawing process is to size tube by shrinking a large diameter tube into a smaller one through a die. Two different types of tube drawing are used in this tube manufacturing process: a mandrel drawing and a tube sinking (without a mandrel inside the tube). The mandrel, which a cylindrical rod around which metal or other material is forged or shaped, is used in the first drawing process to prevent buckling or wrinkling in the tube. The mandrel and the die were represented by rigid surfaces. The tube, with initial dimensions of 1.0 in. OD and 0.102 in. diameter, was drawn to reduce its OD to 0.813" and its thickness to 0.08 in. a first drawing step. The second drawing step shrank the OD to 0.502" while observing a slight increase in the thickness (0.0834 in.).

The following boundary conditions were applied in the first drawing:

- Tube: x-direction moving (front part of tube)
- Die and Mandrel: fixed components (encastred)
- Material Velocity: 33.24 inch/sec (0.76 m/sec)

The friction coefficient of Coulomb between the tube and both the mandrel and die was approximated to 0.05. The DMG ISV material constants were calibrated from the experimental data of post-normalizing.

The mesh of the tube was refined along its circumference to accurately capture the reduction of the outside diameter. With a ratio of element size to tube thickness greater smaller than one, the assumption of thin structures for the use of shell elements was not

satisfied. Both tube drawing processes were simulated 3D solid elements as shown in Figure 29, Figure 30, Figure 32 and Figure 33. Therefore, the 3D solid elements exhibited again a better behavior in terms of contact and thickness prediction than shell elements due to their poor performance for very thick structures.

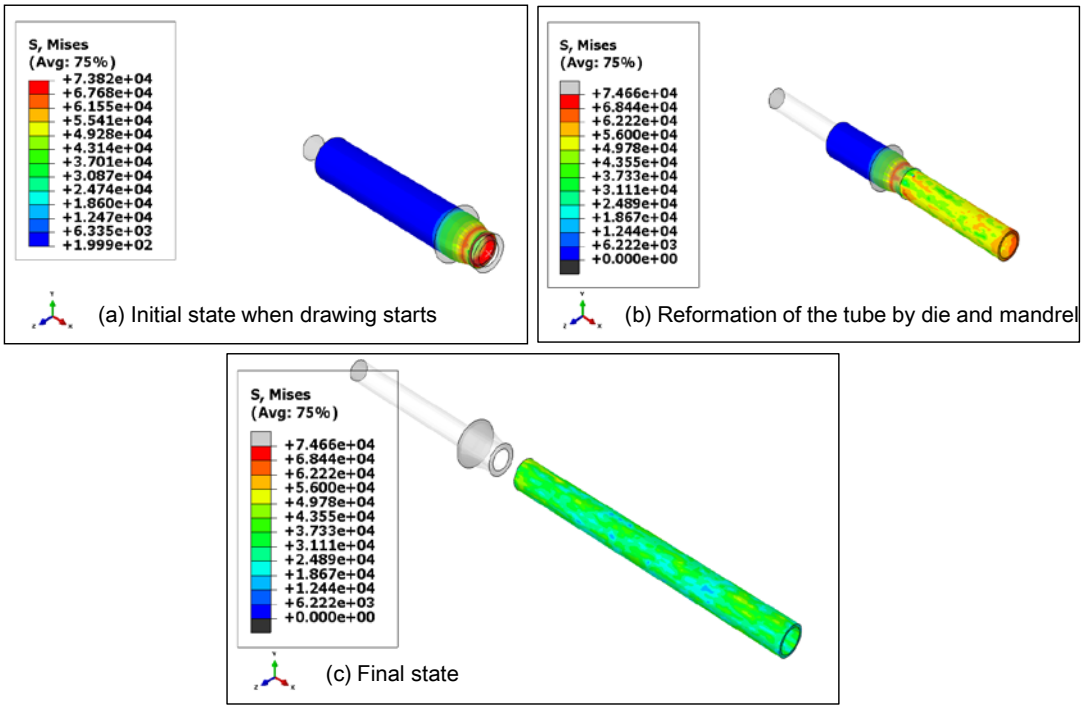

Figure 29. First drawing simulation showing the von Mises stress progression.

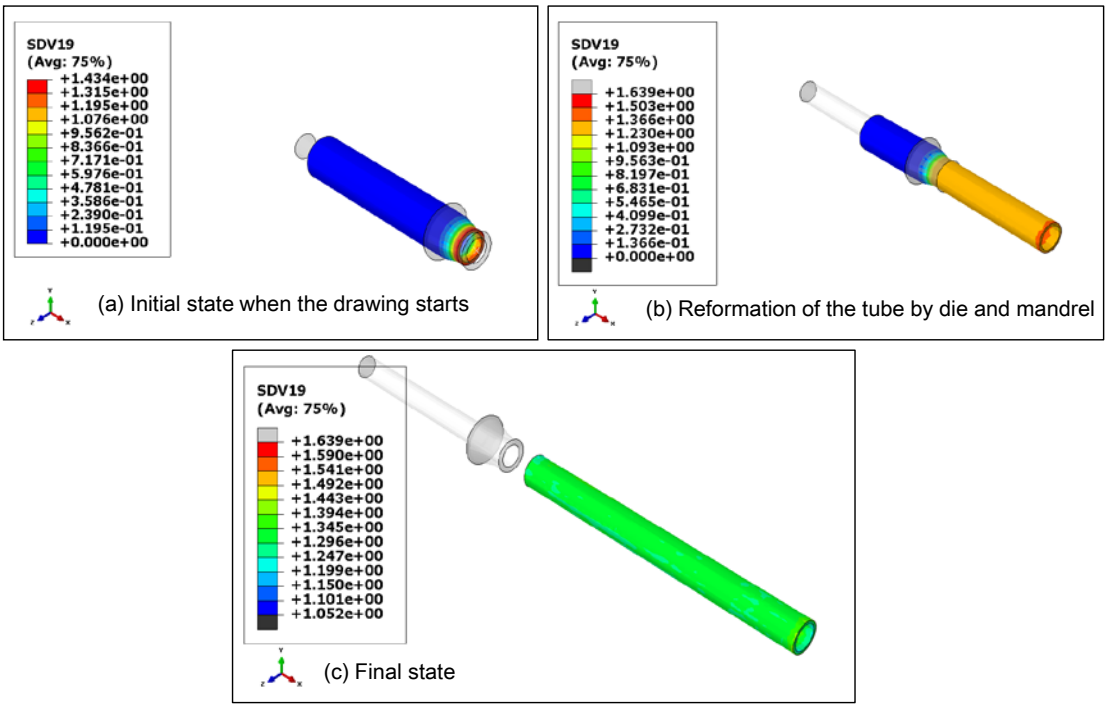

Figure 30. First drawing simulation showing the equivalent plastic strain progression.

Figure 29 and Figure 30 show the von Mises stress and plastic equivalent strain, respectively, at different instant of the first drawing analysis. We can observe that both the Mises stress and the plastic equivalent strain are uniform along the circumference of the tube. The simulation was validated by comparing the post-forming stress-strain behavior with experiments (Figure 31). We observe in the Figure 31 that post-stress-strain curve from the finite element simulation slightly underpredict the experimental ultimate stress probably due to the grain size changes that are currently not accounted for in the ISV model. We will address that in Phase 2.

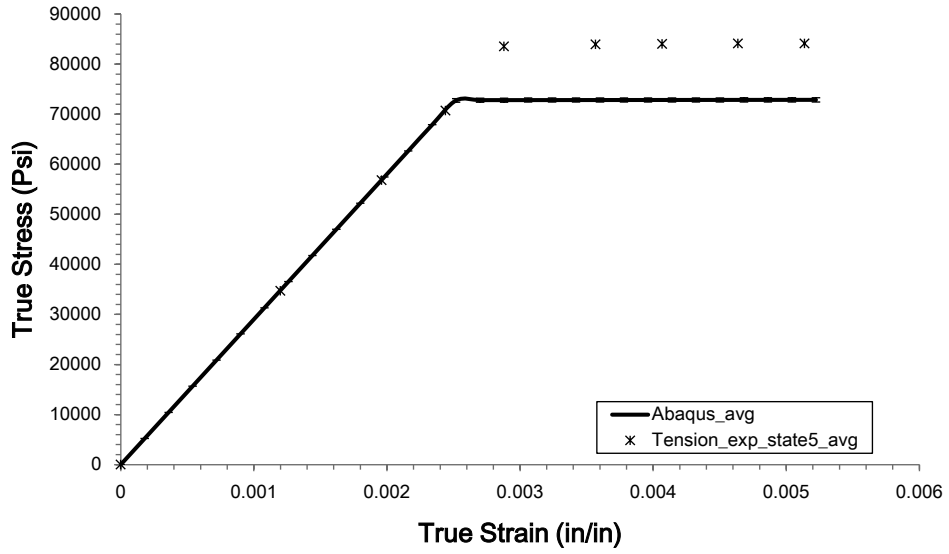

Figure 31. Post-first drawing (State 5) stress-strain behavior: comparison of the finite element model results and experimental data.

In the second drawing simulation with no mandrel, the boundary conditions and coefficient of friction are identical as in the first drawing analysis. The DMG ISV material constants were calibrated from the experimental data of the post-first drawing analysis, whereas if recrystallization were included in the model, this would not be necessary. Again, this will be addressed in Phase 2.

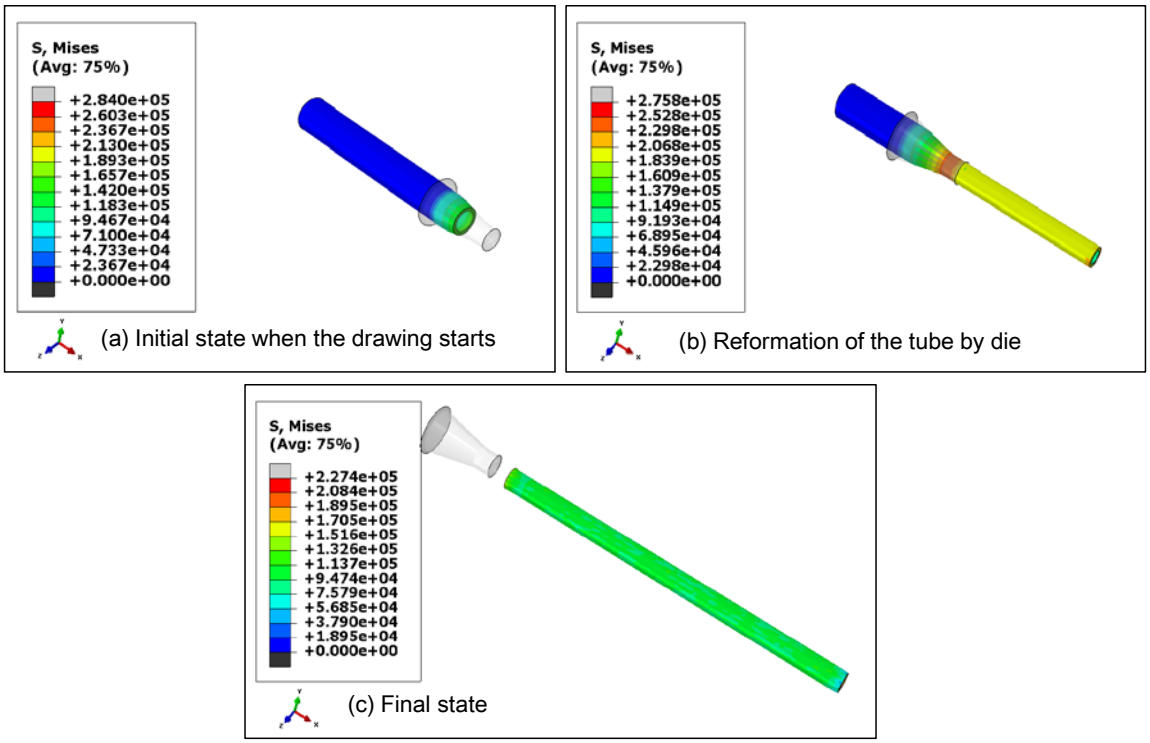

Figure 32. Second drawing simulation showing the von Mises stress progression.

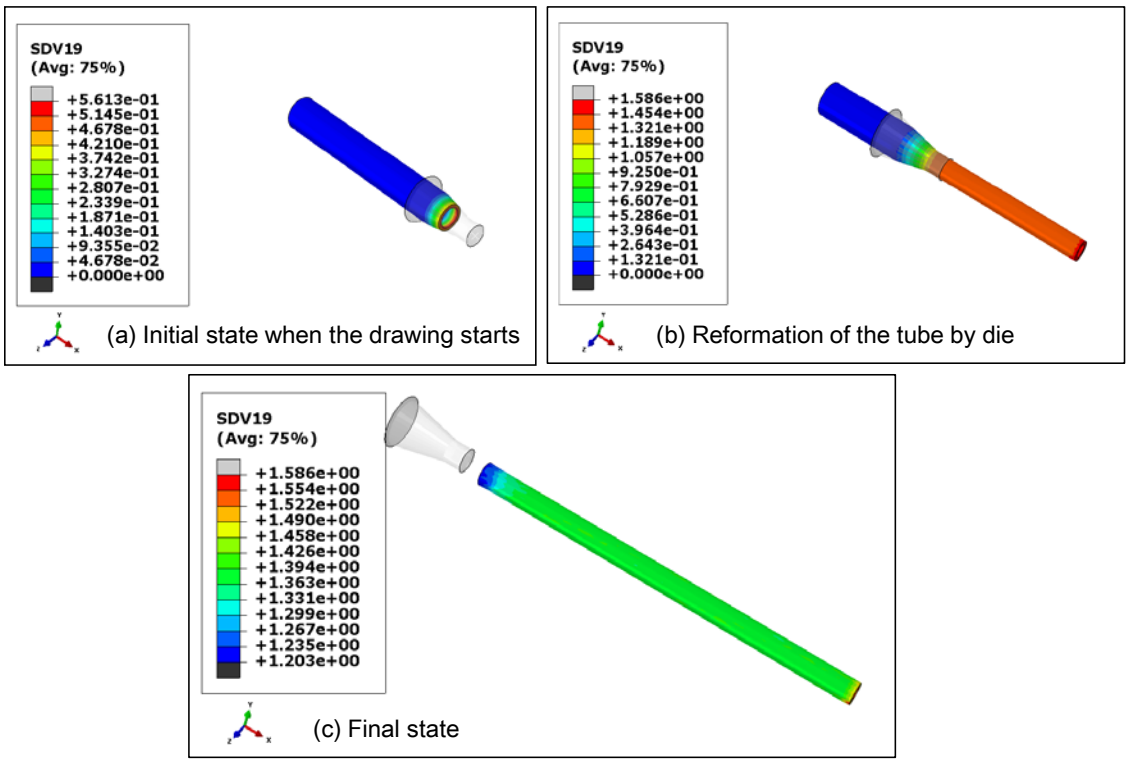

Figure 33. Second drawing simulation showing the equivalent plastic strain progression.

Figure 32 and Figure 33 show the von Mises stress and plastic equivalent strain, respectively, at different instant of the second drawing analysis. The simulation could not be validated due to the overprediction of the ultimate stress in the post-second drawing stress-strain curve (Figure 34). The differences here could be associated with the lack of recrystallization in the model. Again, we will address that in Phase 2.

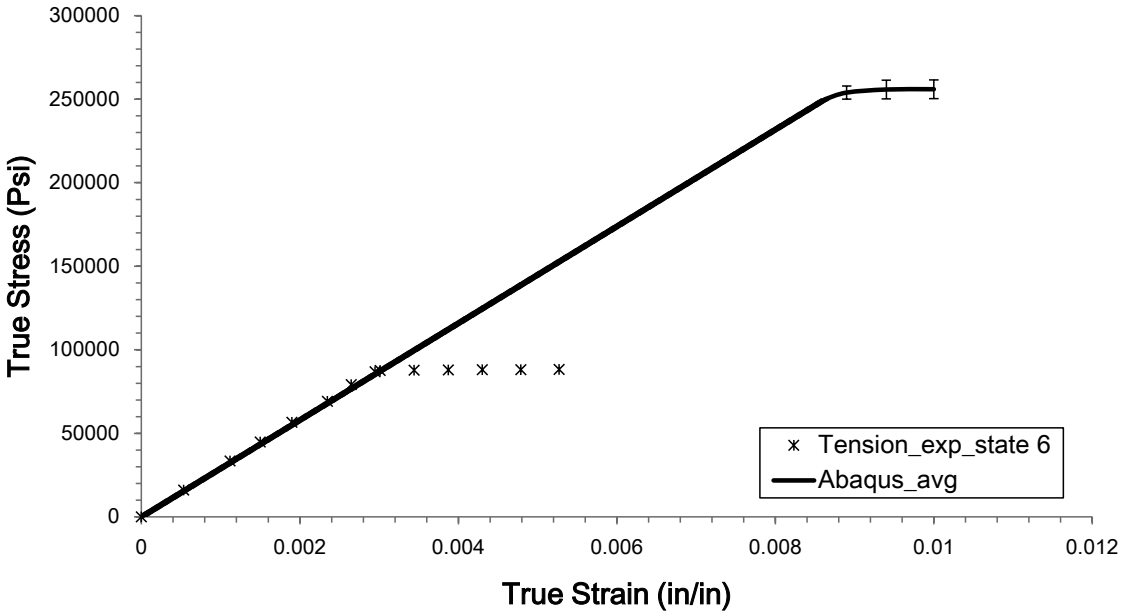

Figure 34. Post-second drawing (State 6) stress-strain behavior: Comparison of the finite element model results and experimental data

5.5 METAMODEL DEVELOPMENT

In this section, the focus is on the tube forming process. Images and discussions regarding metamodel development for the other processes are very similar.

Figure 35 depicts the simulated dataset generated for the tube forming process and its description required by the SUMO software. Basically, the dataset is a rectangular table of numbers representing input-response values. The first columns are the input values, while the rest of the columns are the corresponding response values. The lower half of Figure 5 is a fragment of the file description (in the markup language XML) required by SUMO for the dataset.

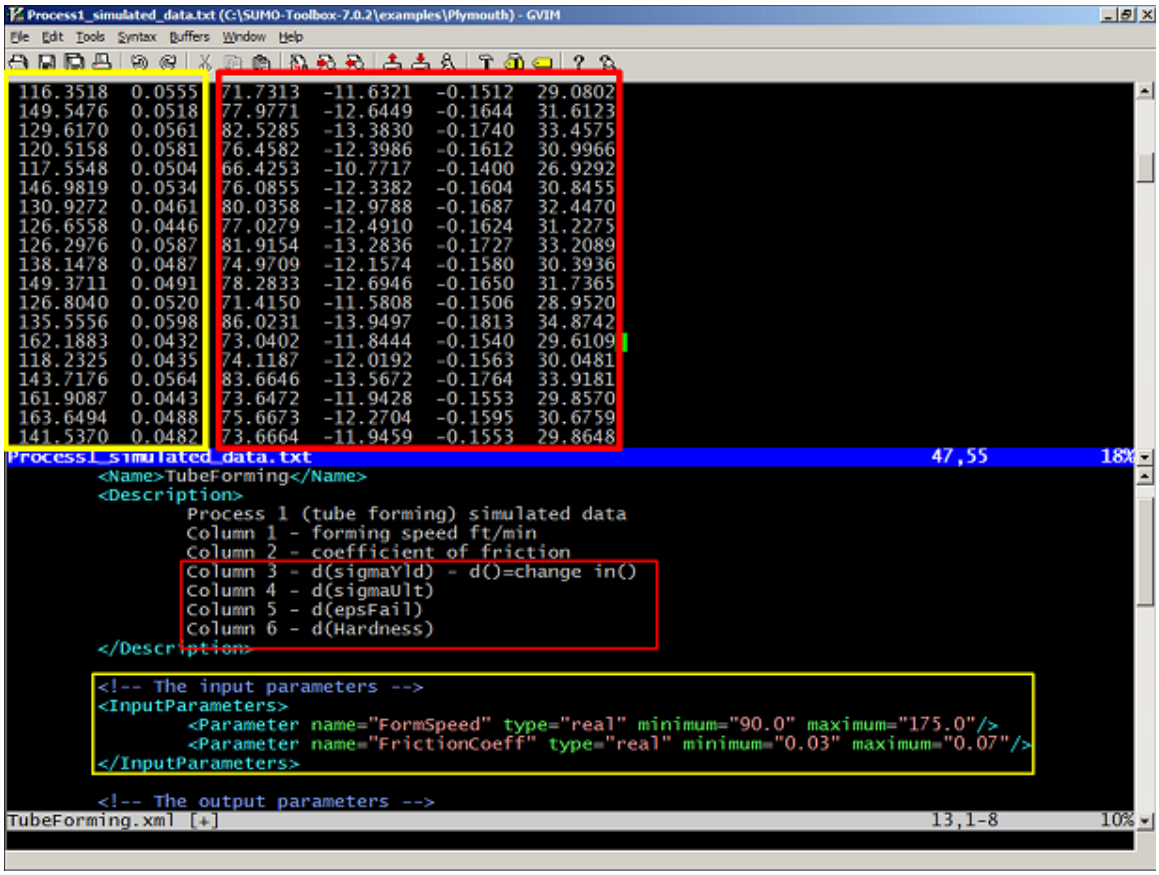

Figure 35. Simulated forming data file and its XML description for SUMO.

Figure 36 shows the listing of a simple SUMO script to build metamodels for the response variables in the generated forming. The script identifies the source of the data to be used (the file above), the model (radial basis functions – RBF), the quality measure (cross-validation), and the error function (root relative square error). These choices seem to be appropriate for the simulated datasets; different choices may be required when building the metamodels for the results of the actual finite element simulations.

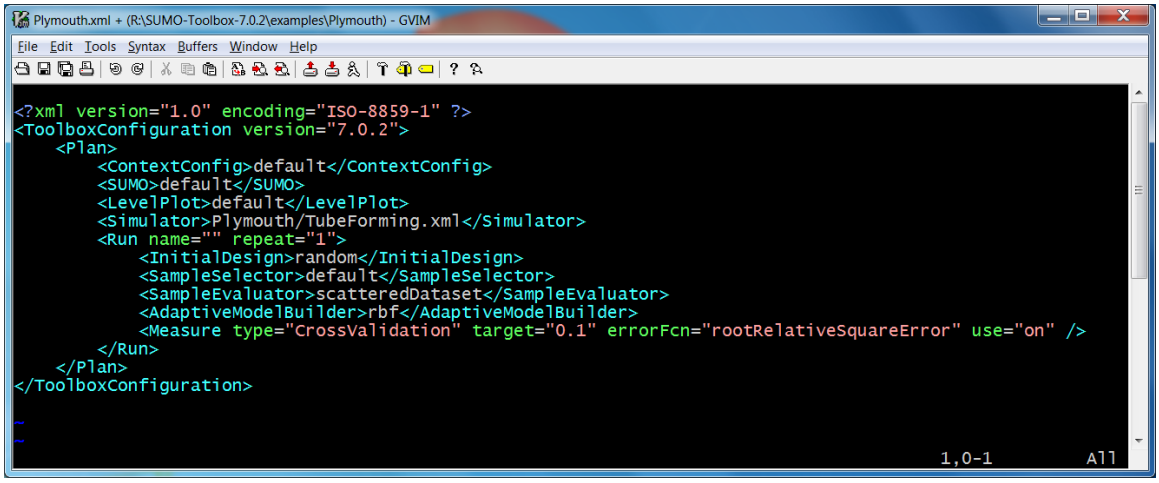

Figure 36. SUMO configuration file to build RBF metamodels for each output variable in the simulated forming data.

Figure 37 visualizes the RBF metamodels derived by SUMO for the response variables in the simulated forming data.

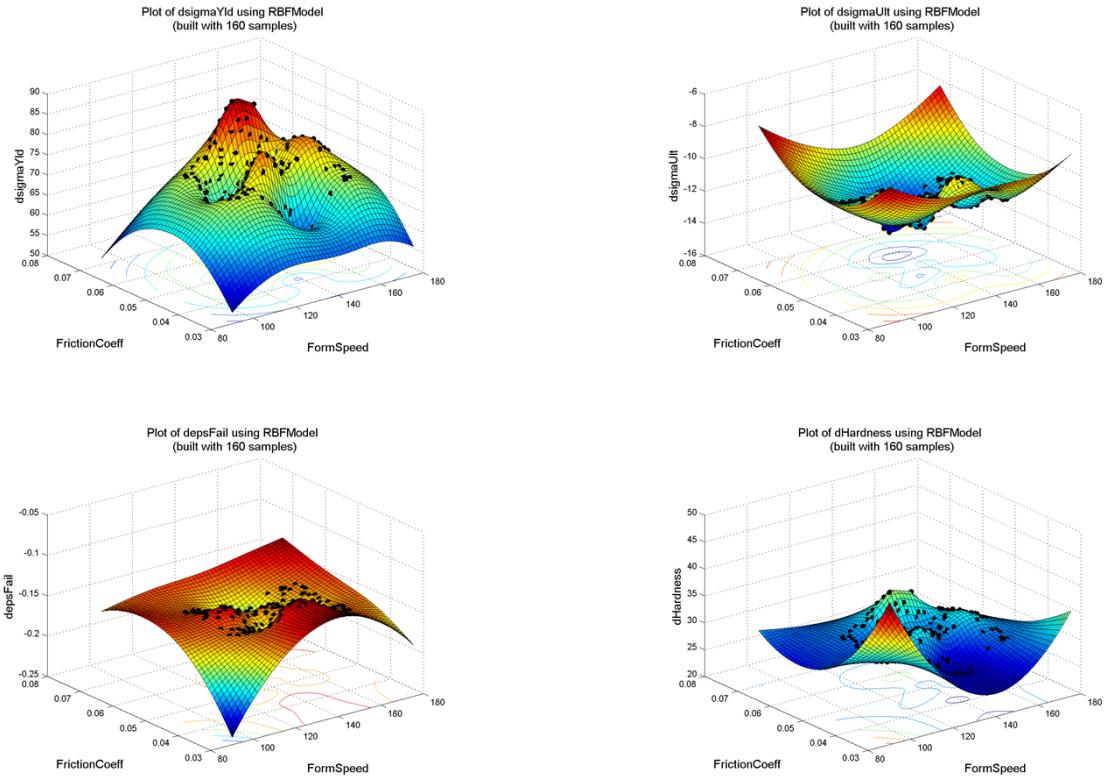

Figure 37. Visualization of the Radial Basis Functions (RBF) metamodels for the simulated forming data.

Figure 38 is a screenshot of the user interface for the software that implements the 'structure-process-properties-cost' relationships in the forming process. The blocks on the

left accept input data: yellow=sheet 'structure' data, orange=forming 'process' data, green=fixed tube 'properties' data. The red blocks on the right accept 'cost' related parameters such as hourly labor rate, electricity consumption, price of electricity, depreciation parameters and others. The blue 'Forming process' block implements the logic to calculate the process time, sheet usage and scrap amount. It also evaluates the metamodel to determine the properties (yield stress, ultimate stress, elongation to failure, and hardness) of the tube coming out of the process. The red blocks implement the logic to calculate costs of labor, equipment, and raw material.

During live demonstration of the software at PTC, the potential end-users identified other costs not yet included in Figure 38, such as chemicals used and other consumables, based on the length or weight of the sheet used. These costs can be added by connecting other red blocks with the appropriate cost calculation logic to the 'sheet_used_ft' or the 'sheet_used_lb' lines.

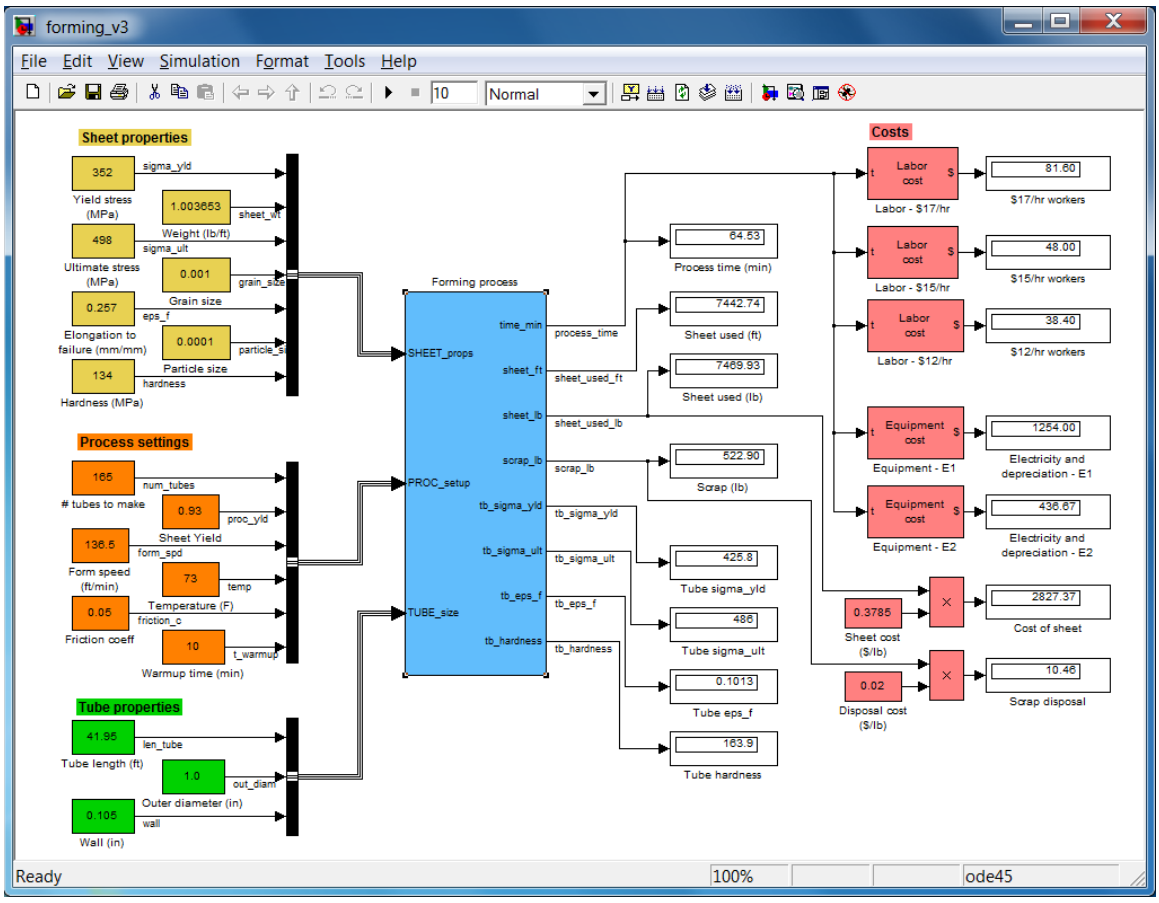

Figure 38. Screenshot of user interface for the code implementing the microstructure-process-property-cost relationships.

Figure 39 is a screenshot of the user interface for the software to determine forming process settings to achieve some desired tube properties. The inputs blocks are similar to those in Figure 38, except that the orange blocks 'Form speed' and 'Friction coeff' are absent – these are quantities to be determined. The desired tube properties are entered via the aqua blocks under 'Tube properties.' The red blocks on the right are the same as in Figure 38. The blue 'Find process settings' block implements the logic to calculate the sheet usage and scrap amount. It also executes an optimization algorithm that evaluates the metamodel to determine values for 'form_spd' and 'friction_c' that will produce the desired properties (yield stress, ultimate stress, elongation to failure, and hardness) of the tube coming out of the process, as well as the corresponding process time. The red blocks implement the logic to calculate costs of labor, equipment, and raw material.

The blue 'Find process settings' block in Figure 39 may return one of many possible combinations of 'form_spd' and 'friction_c' that will produce the same desired tube properties. For demonstration purposes, the block currently uses an optimization algorithm that finds a local optimum. In a later version of the blue block, a global optimization algorithm will be utilized.

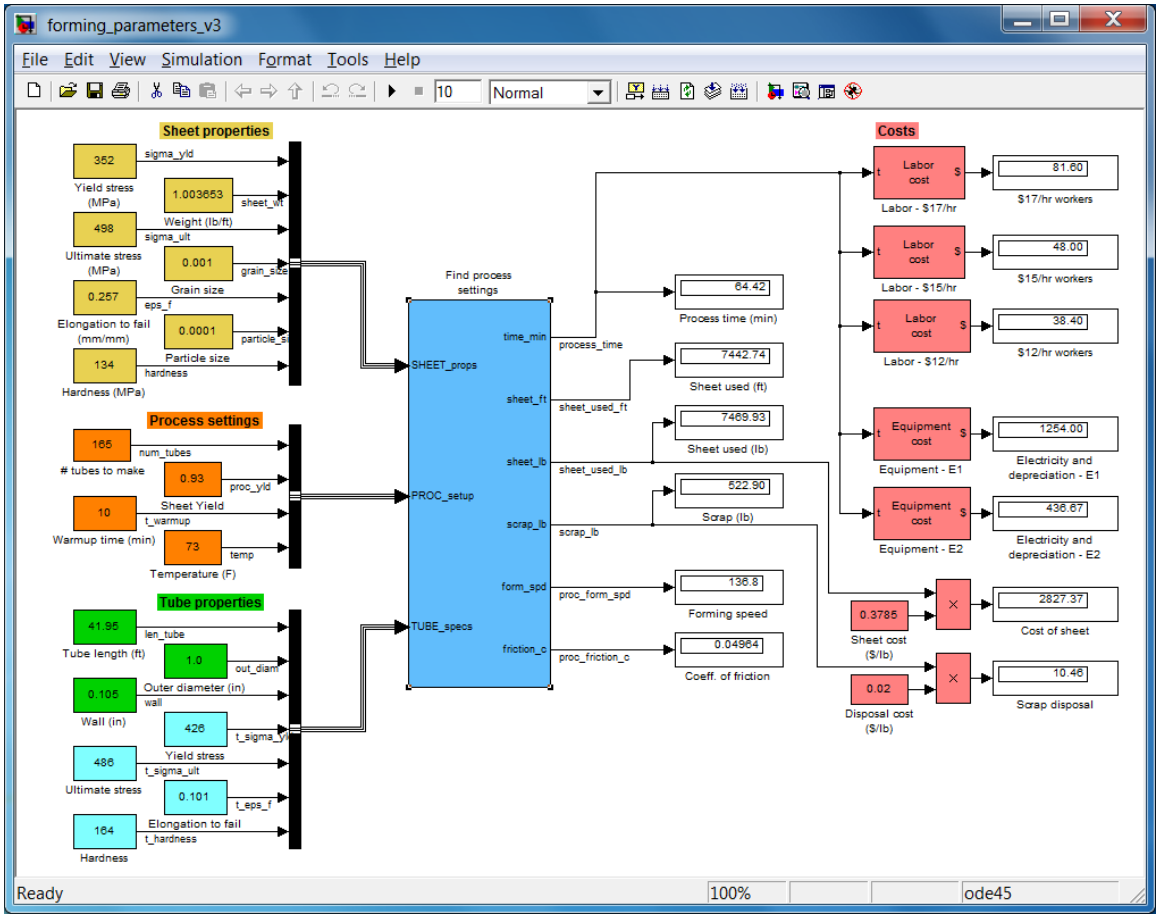

Figure 39. Screenshot of user interface for the code to calculate process settings to achieved desired tube properties.

To account for uncertainties in some inputs, uncertainty parameters will be incorporated as illustrated in Figure 40, using Yield stress as an example. The yellow 'Uncertainty' block outputs a normally distributed random value (Mean=0, Variance=10) that is added to the Yield stress. Other types of random value generators may be used. 'Scope' plots the resulting value 'unc_sigma_yld'; this value will replace 'sigma_yld' in Figure 38 and Figure 39. All the single-value displays (Process time, Sheet used, etc.) will be replaced with scopes to show the effect of the uncertainty in Yield stress. Other relevant inputs may be attached to their own uncertainty parameters; the scopes will show the combined effect of all uncertainties in the selected inputs.

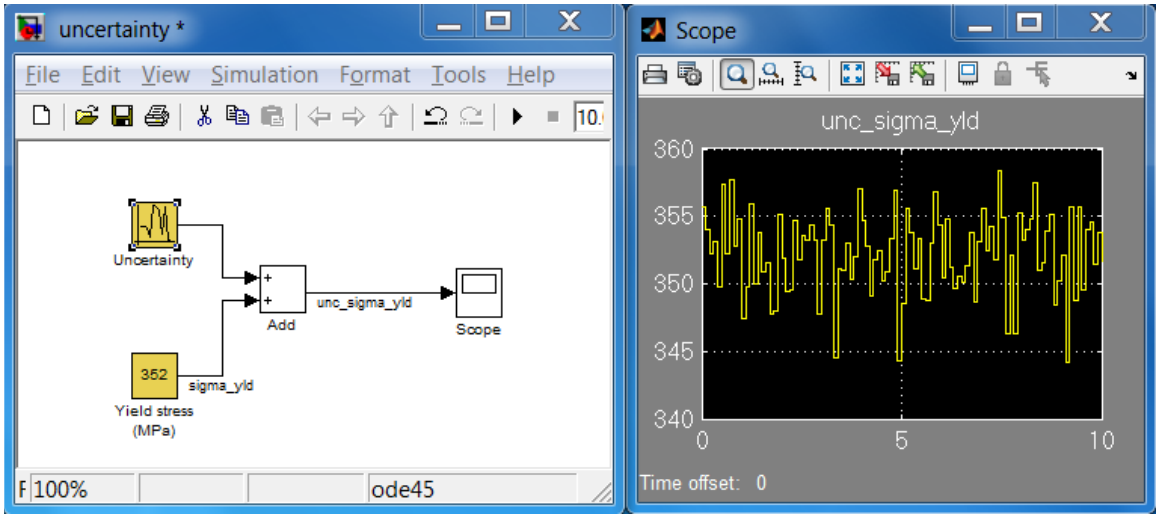

Figure 40. Screenshot of user interface for the code to incorporate uncertainty.

6 CONCLUSIONS

From the research work outlined in this study, the following conclusions can be drawn.

- The cold working experienced during the forming process elongates the grains at the pre-welded slit of the circular tube. This is the location on the tube that has undergone the most strain.
- A phase change from ferrite-pearlite to ferrite-bainite occurs when the tube passes through the high frequency induction welder. This creates a localized brittle zone that is not conducive for tube malleability.
- The heat treatment process that occurs after the tube is welded causes the ferrite grains to recrystallize, ridding the tube of any unwanted residual stresses from cold working and microstructural changes from welding.
- Carbon reacts with oxygen in the atmosphere during the heat treatment process that increases the grain size on the OD of the tube.
- Both drawing processes reduce the grain size in the cross section of the tube and cause the grains to elongate in the rolling direction. During the second draw bench, the grains elongate radially in the cross section orientation because the ID is not constrained by a mandrel.

- Tensile tests show that the microstructure changes experienced during the manufacturing process have a significant role on the stress-strain behavior of the different material states. States with larger grains exhibit longer strain hardening regions, with lower UTS and a greater elongation to failure. In contrast the post cold worked material states have high strength but low ductility.
- Finite element simulation captured most of the sequences of the thermomechanical tube forming. Some issues still need to be addressed, such as:
  - Including uncertainties in the modeling and experimental data;
  - Re-examining the internal state variables and their history dependence with the addition of recrystallization to accommodate the grain size changes; especially in the thermal or thermomechanical loading;
  - Including the damage mechanisms.
- Metamodel Development demonstrates the capability of the PDT-MSU-CAVS-Plymouth project team to build metamodels for tube processing, and to exploit these metamodels in simulating the core activities of the PTC plant. Prototype software that were developed around these metamodels are able to predict process times and costs of labor, material and equipment.
- Based on the work completed in Phase I, in Phase II, PDT proposes to continue to refine the ISV model by correlating and incorporating the uncertainties in the microstructure, mechanical testing, and modeling. Following the model refinement, FE analyses will be simulated and will provide even more realistic predictions as they include an appropriate window of uncertainty. Using the HPC output (FE analyses) as input, the quick-response metamodel codes will more accurately predict and optimize the microstructure-process-property-cost relationships. Furthermore, PDT propose to employ the ICME metamodeling toolkits to help develop a new tube product using entirely new high strength steel. The modeling of the high strength steel manufacturing process will replace the costly and time consuming trial-and-error methods that were used in the tubing industry previously. This simulation-based process prototyping will greatly benefit our industrial partners by opening up new market spaces due to new products with greater capabilities.

7 REFERENCES

Bammann, D.J., Chiesa, M.L., Horstemeyer, M.F., and Weingarten, L.I., (1993), "Failure in Ductile Materials Using Finite Element Methods," eds. N. Jones and T. Weirzbicki, Structural Crashworthiness and Failure, Applied Science.

Benscoter, A. and Bramfitt, B. (2004) Metallography and Microstructures of Low-Carbon and Coated Steels, ASM International, 2004 in ASM Handbook, 588-607.

Budynas, R. and Nisbett, J. (2008) Shigley's Mechanical Engineering Design: Ninth Edition, New York: McGraw Hill , 49.

Cocks, A.C.F., and Ashby,M.F., "Intergranular Fracture during Power Law Creep under Multiaxial Stresses," J. Metal. Sci. Vol. 14, 1980, pp. 395–402.

Davis, J. (1998) Metals Handbook Desk Edition, Second Edition, Materials Park: ASM International, 153-173.

Dieter, G. (1988) Mechanical Metallurgy, New York: McGraw Hill, 646-649.

Gorissen, D., De Tommasi, L., Crombecq, K., Dhaene, T., "Surrogate Modeling (SUMO) Toolbox (v7.0.2)," Springer - Neural Computing & Applications, Vol. 18, N0. 5, pp. 485-494, June 2009.

Horstemeyer, M.F. and Gokhale, A.M., "A Void-crack Nucleation Model for Ductile Material," *Int. J. Solids Struct.*, Vol. 36, 1999, pp. 5029–5055.

Horstemeyer, M.F., Wang, P., "Cradle-to-Grave simulation-Based Design Incorporating Multiscale Microstructure-Property Modeling: Reinvigorating Design with Science," J. Computer-Aided Materials Design, Vol. 10, pp. 13-34, 2003.

Horstemeyer, M.F. Integrated Computational Materials Engineering (ICME): Using Multiscale Modeling to Invigorate Engineering Design with Science, Wiley Press, 2012.

McClintock, F.A., "A Criterion for Ductile Fracture by the Growth of Holes," *J. App. Mech. Trans. ASME*, Vol. 35, 1968, pp. 363–371.

MATLAB version 7.14.0.739 (R2012a), The MathWorks Inc., Natick, Massachusetts, 2010.

Mercier, D., Lesage, J., Decoopman, X. and Chicot, D. (2006) Eddy Currents and Hardness for Evaluation of Steel Decarburizing, NDT&T International 39, 652-660.